



HAL
open science

Photometry of asteroid (101955) Bennu with OVIRS on OSIRIS-REx

Xiao-Duan Zou, Jian-Yang Li, Beth E. Clark, Dathon R. Golish, Salvatore Ferrone, Amy A. Simon, Dennis C. Reuter, Deborah L. Domingue, Hannah Kaplan, Maria Antonietta Barucci, et al.

► **To cite this version:**

Xiao-Duan Zou, Jian-Yang Li, Beth E. Clark, Dathon R. Golish, Salvatore Ferrone, et al.. Photometry of asteroid (101955) Bennu with OVIRS on OSIRIS-REx. *Icarus*, 2021, 358, 10.1016/j.icarus.2020.114183. insu-03713784

HAL Id: insu-03713784

<https://insu.hal.science/insu-03713784>

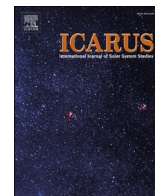
Submitted on 2 May 2023

HAL is a multi-disciplinary open access archive for the deposit and dissemination of scientific research documents, whether they are published or not. The documents may come from teaching and research institutions in France or abroad, or from public or private research centers.

L'archive ouverte pluridisciplinaire **HAL**, est destinée au dépôt et à la diffusion de documents scientifiques de niveau recherche, publiés ou non, émanant des établissements d'enseignement et de recherche français ou étrangers, des laboratoires publics ou privés.



Distributed under a Creative Commons Attribution 4.0 International License



Research Paper



Photometry of asteroid (101955) Bennu with OVIRS on OSIRIS-REx

Xiao-Duan Zou (邹小端)^{a,*}, Jian-Yang Li (李荐扬)^a, Beth E. Clark^b, Dathon R. Golish^c, Salvatore Ferrone^b, Amy A. Simon^d, Dennis C. Reuter^d, Deborah L. Domingue^a, Hannah Kaplan^d, Maria Antonietta Barucci^e, Sonia Fornasier^{e,f}, Alice Praet^e, Pedro Henrique Hasselmann^e, Carina A. Bennett^c, Edward A. Cloutis^g, Eri Tatsumi^{h,i}, Daniella N. DellaGiustina^c, Dante S. Lauretta^c

^a Planetary Science Institute, Tucson, AZ, USA

^b Department of Physics and Astronomy, Ithaca College, Ithaca, NY, USA

^c Lunar and Planetary Laboratory, University of Arizona, Tucson, AZ, USA

^d NASA Goddard Space Flight Center, Greenbelt, MD, USA

^e LESIA, Observatoire de Paris, Université PSL, CNRS, Université de Paris, Sorbonne Université, 921 Meudon, France

^f Institut Universitaire de France (IUF), 1 rue Descartes, 75231 PARIS, CEDEX 05, France

^g Department of Geography, University of Winnipeg, Winnipeg, Manitoba, Canada

^h Instituto de Astrofísica de Canarias, University of La Laguna, La Laguna, Tenerife, Spain

ⁱ Department of Earth and Planetary Science, The University of Tokyo, Bunkyo, Tokyo, Japan

ARTICLE INFO

Keywords:

Asteroid Bennu
Asteroid surfaces
Spectrometer
Photometry

ABSTRACT

NASA's OSIRIS-REx spacecraft arrived at its sampling target, asteroid (101955) Bennu, in December 2018 and started a series of global observation campaigns. Here we investigate the global photometric properties of Bennu as observed by the OSIRIS-REx Visible and InfraRed Spectrometer (OVIRS) over the time period December 9, 2018, to September 26, 2019. In this study we used observations obtained over wavelengths ranging from 0.4 to 3.7 μm , with a solar phase angle range of 5.3° to 132.6°. Our aim is to characterize the global average disk-resolved photometric properties of Bennu with multiple models. The best-fit model is a McEwen model with an exponential phase function and an exponential polynomial partition function. We use this model to correct the OVIRS spectra of Bennu to a standard reference viewing and illumination geometry at visible to infrared wavelengths for the purposes of global spectral mapping. We derive a bolometric Bond albedo map in which Bennu's surface values range from 0.021 to 0.027. We find a phase reddening effect, and our model is effective at removing this phase reddening. Our average model albedo shows a blueish spectrum with a > 10% absorption feature centered at 2.74 μm . Of all comparisons with previously visited asteroids and comets, only 28P/Neujmin, 2P/Encke, and (162173) Ryugu are darker than Bennu. We find that Bennu is a few percent brighter than Ryugu in the wavelengths respectively observed by the OSIRIS-REx and Hayabusa2 missions (from 0.48 to 0.86 μm). We also compare our spectroscopic photometry of Bennu with the OSIRIS-REx imaging photometry and with ground-based predictions.

1. Introduction

NASA's OSIRIS-REx (Origins, Spectral Interpretations, Resource Identification, and Security-Regolith Explorer) asteroid sample return mission (Lauretta et al. 2017) began operating in proximity to near-Earth asteroid (101955) Bennu in December 2018. Golish et al. (2020) reported on the global photometry of Bennu based on imaging data from the OSIRIS-REx Camera Suite (OCAMS; Rizk et al. 2018) onboard the

spacecraft. Here we present a complementary analysis of the global photometry of Bennu from measurements by the OSIRIS-REx Visible and InfraRed Spectrometer (OVIRS; Reuter et al. 2018). This instrument is a point spectrometer with a wedged filter design, with heritage from the New Horizons LEISA (Linear Etalon Imaging Spectral Array) instrument.

Photometric modeling is a tool for quantitative study of the light-scattering properties of a surface. We can infer or compare surface physical properties such as porosity, composition, particle size, and

* Corresponding author.

E-mail address: zoux@psi.edu (X.-D. Zou).

<https://doi.org/10.1016/j.icarus.2020.114183>

Received 30 May 2020; Received in revised form 1 October 2020; Accepted 22 October 2020

Available online 10 November 2020

0019-1035/© 2020 The Authors. Published by Elsevier Inc. This is an open access article under the CC BY license (<http://creativecommons.org/licenses/by/4.0/>).

roughness from the photometric properties. Light-scattering properties can be described by models of reflectance and viewing geometry that include incidence angle (i , the angle between the direction of the illumination source and the surface normal), emission angle (e , the angle between the direction to the detector and the surface normal), and phase angle (α , the Sun-asteroid-spacecraftobserver angle). Photometry is a tool for quantitative study of the light-scattering properties of a surface. We can infer or compare surface physical properties such as porosity, composition, particle size, and roughness from the photometric properties. The light-scattering amount and ratio can be described by models of reflectance and viewing geometry, including incidence angle (i , the angle between the direction of the illumination source and the surface normal), emission angle (e , the angle between the direction to the detector and the surface normal), and phase angle (α , the Sun-asteroid-spacecraft angle).

This work focuses on OVIRS data acquired from December 9, 2018, to September 26, 2019. Section 2 introduces the observations, calibration, and reduction details of the dataset. In section 3, we describe our disk-resolved photometric models and analyze our results. We provide model uncertainty estimates, estimates of the precision of photometric correction, and maps of the bolometric Bond albedo. In section 4, we discuss the phase reddening effect, how our findings relate to other photometric studies of Bennu, and how Bennu's photometric properties compare with those of other asteroids. In Section 5, we summarize the main findings of our work.

2. Dataset

OVIRS is used for the spectral characterization of the surface of Bennu, with a field of view of 4 mrad and an effective spectral range from 0.4 to 4.3 μm . Because the reflected solar signal is very low longward of 3.7 μm , the spectral region from 3.7 to 4.3 μm is noisy, and we limit our analysis to the spectral range from 0.4 to 3.7 μm . After converting to radiance units, the OVIRS spots were resampled onto a common wavelength axis with a spectral sampling of 0.2 μm from 0.4 to 2.4 μm and 0.5 μm from 2.4 to 4.3 μm . The spectral resolution is a function of wavelength and is given in Reuter et al. (2018). The calibration and performance of OVIRS was validated by Simon et al. (2018) with the OSIRIS-REx Earth flyby data collected in 2017.

2.1. Mission phases and observation conditions

The OSIRIS-REx mission is designed to perform observations in a progression of science phases (Lauretta et al. 2017). These science phases, in chronological order, are Approach, Preliminary Survey, Orbital A, Detailed Survey–Baseball Diamond (BBD), Detailed Survey–Equatorial Stations (EQ), Orbital B, Orbital C, Reconnaissance (Recon), and rehearsals for the Touch and Go (TAG) sample acquisition event. More details about the OSIRIS-REx mission phases can be found at the mission website (www.asteroidmission.org/asteroid-operations/) and in Lauretta et al. (2017).

The OVIRS instrument started observing Bennu on November 2, 2018, during the Approach phase (Hamilton et al. 2019). Bennu was smaller than the 4-mrad OVIRS field of view (FOV) during Approach, except on the last day of this phase (December 2), when OVIRS obtained spectra at a footprint diameter of 92 m. Although OVIRS obtained 851 spots on December 2 with Bennu filling the spectrometer FOV, these observations were affected by off-nominal detector temperatures and non-optimal viewing conditions; hence, our dataset begins with spectra obtained between December 9 and December 17 during the Preliminary Survey.

BBD and EQ observations were also affected by off-nominal temperatures to some degree but had higher flux owing to Bennu's proximity to the Sun, resulting in better overall observing conditions. However, with the asteroid being closer to perihelion, some spectra collected in the early afternoon (local solar time) were saturated by

thermal flux and are thus excluded from this study. We use data from three of the mission's seven BBD flybys. The second BBD flyby (BBD2) was repeated during the Recon phase to observe northern hemisphere regions that were missed on the initial attempt (due to a communication outage). For OVIRS, the conditions during this re-fly were an improvement over the first attempt when the detector and surface were warmer, so we use the re-fly data and exclude the first attempt. We use data from all seven EQ observations, which were each performed at different local solar times. Table 1 gives the observation conditions for all of the datasets that were used.

Hence, this study comprises the global observation data from Preliminary Survey, BBD, and EQ. We start with a total of 299,702 calibrated spots and we selected 70,342 spectra for photometric modeling. Table 1 lists the observational conditions under which these data were collected. The data selection (based on data quality) of numbered EQ stations, their local time and observational geometry are introduced in section 3.1.

To investigate the global average photometric properties of Bennu from OVIRS data, we use the viewing geometry output from the standard processing and pointing calculations of the OSIRIS-REx ground pipeline, executed by the OSIRIS-REx Science Processing and Operations Center (SPOC) (Selznick 2017). The incidence and emission angles are derived by calculating the average angular properties of 100 vectors uniformly distributed within the OVIRS FOV. The angular data we use are based on Bennu shape model v20 (version 20) produced using stereophotoclinometry by Barnouin et al. (2019). This shape model has a resolution of ~ 0.8 m per triangular facet, but it can be degraded to more closely match an instrument's spatial resolution. The average facet edge length in our Bennu shape model for OVIRS data analysis was thus degraded to 3 m. Compared to the average spot size during EQ, ~ 20 m, this means that on average, we are accounting for ~ 280 facet elements per OVIRS footprint.

2.2. Calibration procedure from instrument data to radiance units

The OVIRS FOV is 4-mrad in diameter, and each spectrum represents a single spot projected onto the target asteroid, such that the range to the target determines the spot size. A spectrum is made using five linear variable filter segments to cover the full spectral range, as described in Reuter et al. (2018). The calibration and performance of OVIRS was validated by Simon et al. (2018) with the OSIRIS-REx Earth flyby data and updated during the encounter at Bennu (Simon et al. 2020). Our ground calibration pipeline converts the raw data (counts per second) to physical units ($\text{W}/\text{cm}^2/\text{sr}/\mu\text{m}$) and then to spot I/F (radiance factor, RADF).

In this process, the background is subtracted first. Then, the out-of-band (IR leak) contributions are calculated and removed from the spectra. After converting to radiance units, the OVIRS spots are resampled onto a common wavelength sampling, with a spectral resolution of 0.2 μm from 0.4 to 2.4 μm and 0.5 μm from 2.4 to 4.3 μm . The component of the radiance due to the thermal emission of the target is removed by fitting and subtracting the short wavelength tail of a single temperature blackbody curve. Finally, the radiance value is divided by solar incident flux to obtain the RADF "Level 3" data (Simon et al. 2020).

Before beginning our photometric modeling, we evaluated the phase angle dependence of calibrated OVIRS data by ratioing spectra of the same general location on the surface of Bennu obtained at two different phase angles. We show an areal mean ratio of the spectra from EQ3 (7° phase angle) and EQ4 (30° phase angle) in Fig. 1. We selected spots that spatially cover a $10^\circ \times 10^\circ$ (lat, lon) area at each of five different latitudes (0°, 15°, 30°, 45° and 60°) for the ratio comparison. Because both EQ3 and EQ4 are observed at narrow phase angle ranges, the ratio of the overlapping spots from these two stations is approximately the phase ratio of our calibrated data. When we calculate a phase ratio, we expect generally low-frequency gentle wavelength dependence, such as phase reddening. We can also see sharper wavelength dependencies inside

Table 1

Characteristics of the OVIRS spots used in the photometric analysis, including from Preliminary Survey, Detailed Survey BBD flybys, and Detailed Survey EQ stations. A spot 100% filled means that Benu fills the entire FOV. The original BBD2 data are described in this table but are not included in our analyses due to poor data quality. EQ3 and EQ6 included observation targeting to constrain Benu's thermal emission phase function (TEPF). The EQ2 and EQ5 campaigns included off-nadir pointing for one-quarter of Benu's rotation to constrain the solar reflectance phase function.

Observation	DOY (Day of year)	Date (MM/DD/ YYYY)	Range (km)	Phase range ($^{\circ}$)	Spatial resolution (m)	No. of calibrated spots	No. of spots 100% filled	No. of spots with i $\leq 70^{\circ}$ $e \leq 70^{\circ}$
Preliminary Survey	343	12/09/2018	11.25	91.26–92.05	44	17,333	1265	542
Observations	346	12/12/2018	9.95	37.75–52.03	40	17,018	10,794	9110
	347	12/13/2018	9.88	38.33–51.87	40	17,935	2598	2076
	350	12/16/2018	11.26	90.07–90.35	44	17,237	2536	22
	351	12/17/2018	11.01	89.76–91.27	44	17,049	2236	498
BBD1	66	03/07/2019	4.73	5.63–10.13	19	17,248	16,971	16,327
BBD3	80	03/21/2019	3.58	30.05–31.34	14	17,017	17,017	16,167
EQ1	115	04/25/2019	4.87	43.00–48.01	20	22,622	8836	7557
EQ2	122	05/02/2019	4.85	132.44–132.53	20	16,537	5786	27
EQ2 off-nadir	123	05/03/2019	4.97	129.24–131.39	20	3941	856	381
EQ3	129	05/09/2019	4.8	7.75–10.37	19	17,790	7193	7151
EQ3 TEPF	131	05/11/2019	5.33	51.05–62.63	21	21,572	7502	4270
EQ4	136	05/16/2019	4.75	29.68–30.43	20	15,267	6189	6050
EQ5	143	05/23/2019	4.76	90.22–92.56	20	16,836	6394	805
EQ5 off-nadir	146	05/26/2019	4.28	76.99–88.29	17	15,511	7658	3168
EQ6	150	05/30/2019	4.95	132.03–132.62	20	9787	3514	7
EQ6 TEPF	151	05/31/2019	5.22	127.93–130.91	21	3198	704	484
EQ7	157	06/06/2019	4.87	90.22–93.33	20	9775	3872	266
BBD2 (re-fly)	269	09/26/2019	3.6	7.93–10.75	17	8227	8227	8227

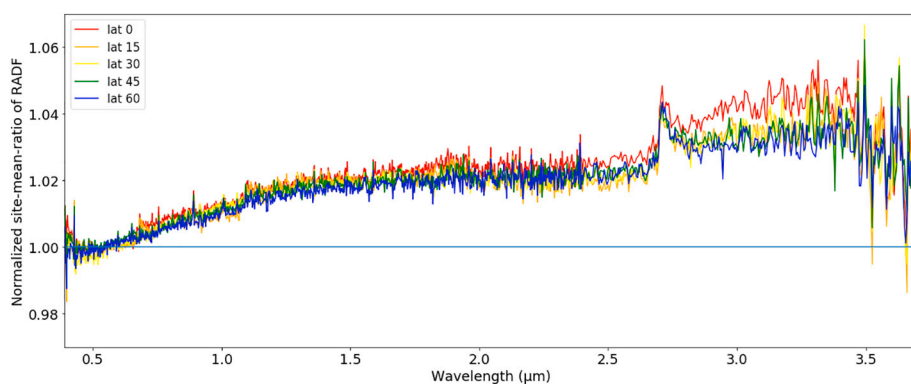


Fig. 1. Ratio (EQ4/EQ3) of averaged spectra within five $10^{\circ} \times 10^{\circ}$ (lat, lon) areas at different latitudes (shown in different colors) centered at 90° longitude. The ratios are normalized to 1.0 at $0.55 \mu\text{m}$. Phase ratios are generally expected to show low-frequency gentle wavelength dependence, such as a linear slope due to phase reddening, as observed here. Inside deep absorption features, we expect sharper wavelength dependencies in the phase ratio, as observed in the $2.74\text{-}\mu\text{m}$ feature. In these data, there are also small jumps at filter segment boundaries, and a bump-shaped feature in the range from 2.9 to $3.7 \mu\text{m}$; these features are observed in the calibrated OVIRS spots, the input data for photometric modeling.

absorption features in a phase ratio. Fig. 1 shows both of these expected properties, but we also see filter segment-related discontinuities (e.g. at 0.66 and $1.1 \mu\text{m}$) and a bump-shaped feature from about 2.9 to $3.7 \mu\text{m}$ (strongest at the equator). These features are not included in the error estimations for the calibrated data that we use as input, but they are taken into account when we discuss the phase ratio properties of Benu and the photometric correction uncertainties in later sections.

3. Disk-resolved photometry with empirical models

3.1. Data selection

The data were filtered to select spectra with the highest quality for use in the photometric model. To construct our input dataset for photometric modeling, we follow these steps: (1) Select only OVIRS spots where Benu fills the FOV (i.e., 100% filled in Table 1) because the unfilled spots are not calibrated. (2) Remove spots with incidence or emission angles greater than 70° (Table 1) due to poor data quality and restrictions in our disk-function modeling ability. (3) Exclude all spectra with noise spikes ($>1.2 \times$ mean value) or negative values due to saturation at the longest wavelengths. (4) Exclude all spectra with jumps $>10\%$ at filter segment boundaries (Fig. 2). After all steps of our data selection process, we selected 70,342 spectra out of 299,702 from the datasets that we considered. (see Table 1 final three columns for the

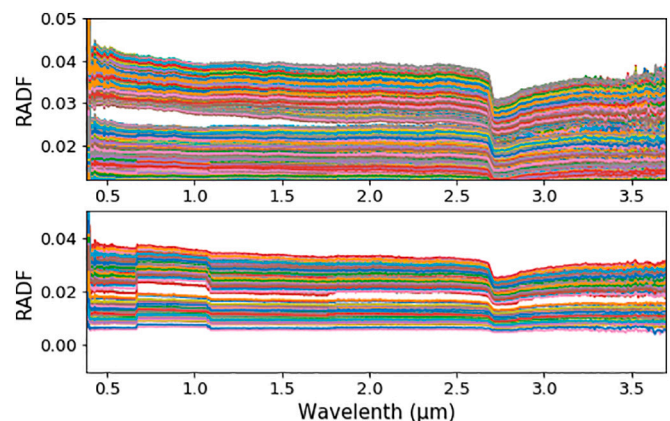


Fig. 2. Representation of the spectra filtered out for excessive segment discontinuity from 0.66 to $1.7 \mu\text{m}$. Top: randomly colored spectra with low spectral discontinuities, included in our photometric modeling dataset. Bottom: spectra with $>10\%$ segment discontinuities (most often at 0.66 and $1.07 \mu\text{m}$), excluded from our modeling dataset. The 132 spots we rejected at this step are mostly from high-latitude areas (latitude $>75^{\circ}$) and are due to the filter segments crossing the illuminated limb at different times.

break down).

Fig. 3 shows density plots (counts of spectra) with respect to both latitude and RADF after data selection. In phase angle space, the largest concentrations of data points are within phase angle ranges 6° to 10° (34% of spots), 30° to 31° (23% of spots) and 38° to 63° (33% of spots). The phase function model is therefore dominated by the data at these phase angles. There are also two data point clouds at 77° to 93° (8%) and 127° to 132° (1%). Because of the large span in phase angles from 6° to 132° , the uneven weighting caused by the distribution of data points between 6° and 63° should not create any strong biases in our modeling process. The incidence and emission angles of our data cover the full range of illumination and viewing geometries.

In Fig. 4, we show the observational strategy employed during EQ. Fig. 5 shows the resulting spatial coverage of the OVIRS spots selected for photometric modeling. These three maps show the geometry sampling biases relative to the global area: (1) the north and south polar

regions (latitudes higher than 75°) are not fully covered, and (2) observations of low-latitude regions have lower incidence and emission angles.

The maps we present in Fig. 5 show only data selected for photometric modeling after the filtering steps described above. The highest-phase-angle observations obtained come with high incidence and emission angles, such that when we apply our filter we find that the highest phase angle spots are restricted to the northern hemisphere of Bennu. Because most data were obtained with the spacecraft located near the equatorial plane of the asteroid and scanning along the meridian in the north-south direction, as shown in Fig. 4, there is a dependence of both incidence and emission angle on latitude. As such, the equatorial region on Bennu is mostly observed at low incidence and emission angles, while higher incidence and emission angles are achieved for higher-latitude regions. This distribution could potentially confuse latitude-dependent reflectance with disk-function behavior (see

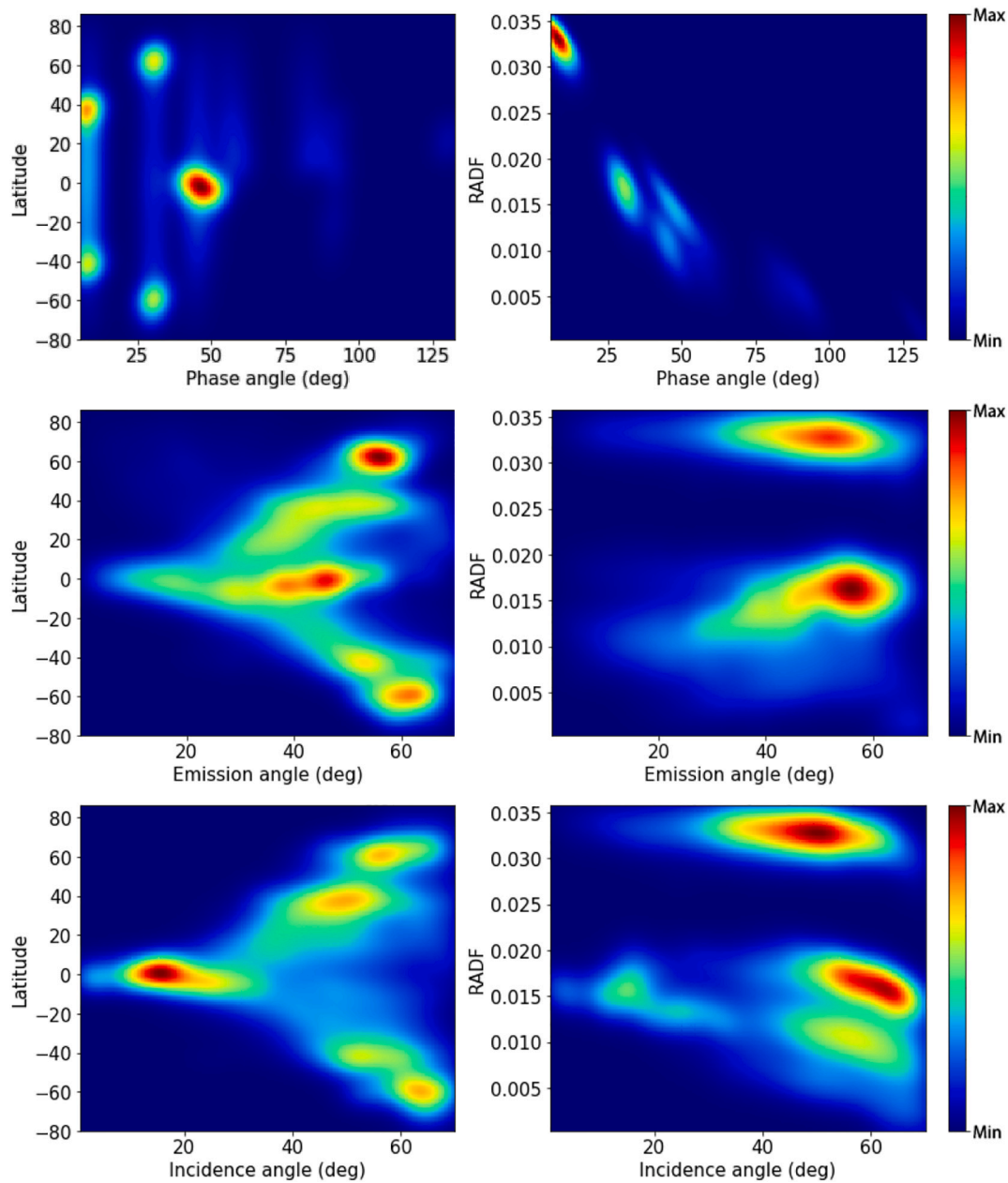


Fig. 3. Density of the OVIRS spots selected for the photometric analysis, smoothed assuming Gaussian-like distributions. Spots with large incidence and emission angles ($i > 70^\circ$, $e > 70^\circ$) are not included. The lowest observational phase angle is 5.3° , and the highest is 132.6° . (The minimum values are all zero, and the quantitative explanations of the maximum values are in the supplementary materials.)

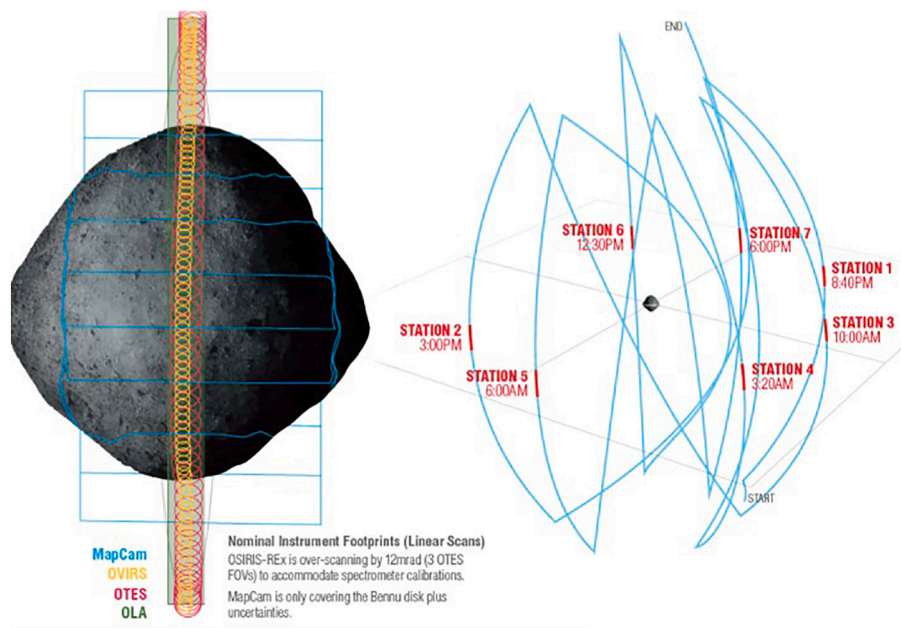


Fig. 4. OVIRS observations during EQ. (Left) The observational strategy employed during EQ. (Right) Our photometric modeling dataset incorporates observations from all seven EQ stations, shown schematically with respect to Benu surface local solar time. (Credit: Heather Roper, University of Arizona).

Section 3.2 for details of the photometric models), and we would not be able to resolve the ambiguity. We compare the albedo maps produced by our photometric model from OVIRS data with those based on OCAMS to assess this effect. We also consider the spatial bias of our geometry sampling later, when we discuss the representativeness of our global average photometric models of Bennu.

In Fig. 6, we show the phase function (phase curve) of our photometric modeling dataset, after application of a simple parameter-less Lommel-Seeliger disk function correction. There are a small number of data points with low phase angle ($5.2^\circ < \alpha < 11.5^\circ$), at high incidence angles ($i > 60^\circ$) and moderate emission angles ($30^\circ < e < 70^\circ$). The incidence angles of these data points suggest that they are from high latitudes and/or shadowed areas inside large craters, or on the sides of large boulders, and likely have non-zero values owing to low-incidence light falling on crater walls. Although we consider these spectra to be of questionable relevance, we do not discard them from our modeling. Sources of uncertainty in the pointing calculations may include incorrect projection of the spectrometer footprints or incomplete filling of the FOV (these values are each calculated from the mid-exposure point; they neglect along-track smear, and it is not always determined if the FOV is off the surface for part of the exposure).

3.2. Empirical models

Our photometric analysis of Bennu is a global average study of the scattering behavior measured at every OVIRS channel (total 1265) over the wavelengths from 0.4 to 3.7 μm . In taking this approach, we assume that Bennu's photometric properties are globally uniform at each wavelength. Hergenrother et al. (2013) published the first ground-based disk-integrated study and HG model fit, and Takir et al. (2015) followed with empirical and Hapke model fits to the same dataset. Hasselmann et al. (2020) model the first-order scattering processes from the rough surface of Bennu using a semi-numerical statistical model developed by Van Ginneken et al. (1998). Their work is most relevant to comparisons with Hapke modeling results from Bennu, which will be presented in our later reports. As noted earlier, Golish et al. (2020) presented global average photometry of Bennu from OCAMS, specifically the MapCam images; they favored a ROLO (Robotic Lunar Observatory) model over several others explored. The Takir et al. (2015) and Golish et al. (2020)

studies share many similar techniques and methods with our work. For example, similar to Golish et al. (2020), we explore a suite of empirical photometric models — in our case: Lommel-Seeliger (Hapke 2012), Minnaert (Takir et al. 2015), McEwen (McEwen 1986), and two forms of the Akimov model (Shkuratov et al. 2011; Li et al. 2019, 2020), as listed in Table 2 each with its formula. We fit all models to the same OVIRS dataset described in the previous section and compare the resulting fits in terms of quality to select a best-fit model. Before settling on a model-fitting routine, we bin the data in various ways — according to viewing and illumination angles — to find a good balance between the computational efficiency and model fidelity. The wavelength dependence of Bennu's photometric properties is established by independently fitting each OVIRS channel. (See Table 2.)

We express our photometric functions in units of RADF (Hapke 2012). We use the symbols i , e , and α to express the incidence, emission, and phase angles, respectively. Photometric latitude and longitude are b and l , respectively. To calculate photometric latitude and longitude, we follow the formalism of Kreslavsky and Head III (2000) (see Golish et al. 2020; and Fig. 1 of Shkuratov et al. 2011)

$$\tan(l) = \frac{\frac{\cos(i)}{\cos(e)} - \cos(\alpha)}{\sin(\alpha)}$$

$$\cos(b) = \frac{\cos(e)}{\cos(l)}$$

A_{XX} is the model-determined global average albedo for each function XX . All other parameters in Table 2 are function coefficients derived by our model fitting; we use distinct symbols for each functional form.

In Table 2 we list the two main components of every photometric model: a disk function and a phase function. The disk function captures the dependence of reflectance on incidence and emission angles, and the phase function captures the dependence on phase angle. Our form of the McEwen model uses an exponential phase function. For first-order photometric corrections when phase angle is approximately constant, it can be useful to use a parameter-less disk function, such as in the Akimov and Lommel-Seeliger models. However, when phase angle is not constant, or when the parameter-less disk functions fail to describe the scattering properties of a surface, empirical models with free parameters in the disk function, such as the McEwen and Minnaert models, are

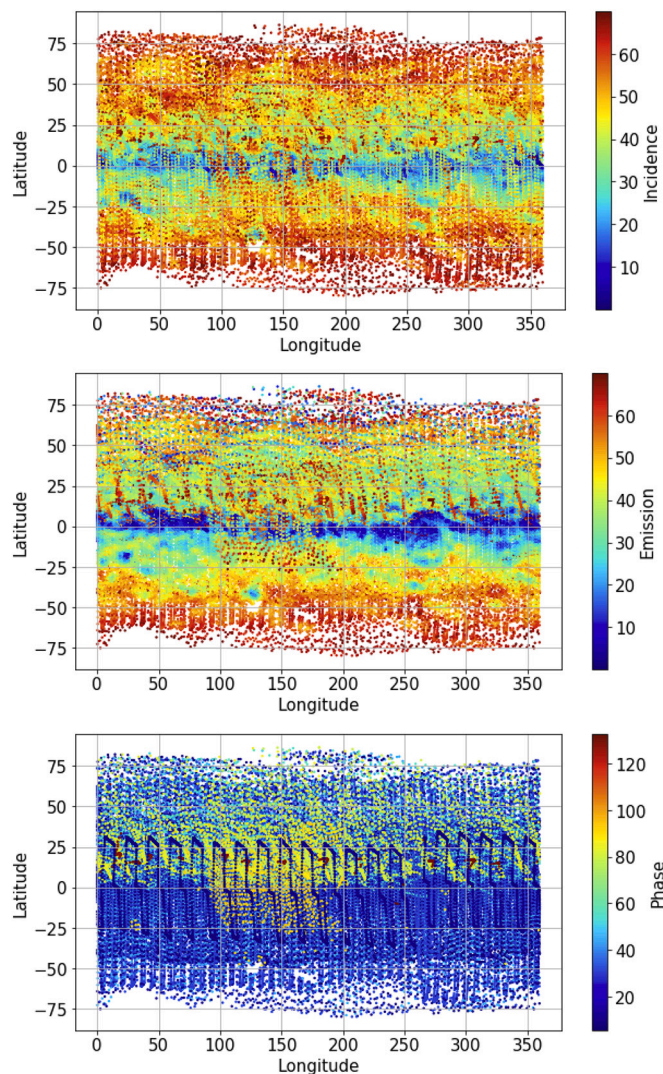


Fig. 5. Spatial coverage of the selected OVIRS dataset according to the distributions of (top) incidence angle, (middle) emission angle, and (bottom) phase angle. Our dataset covers the surface of Bennu between $+75^\circ$ and -75° latitude. The observation strategy led to asymmetries between geometries in the northern and southern hemispheres, especially with respect to incidence and emission angles.

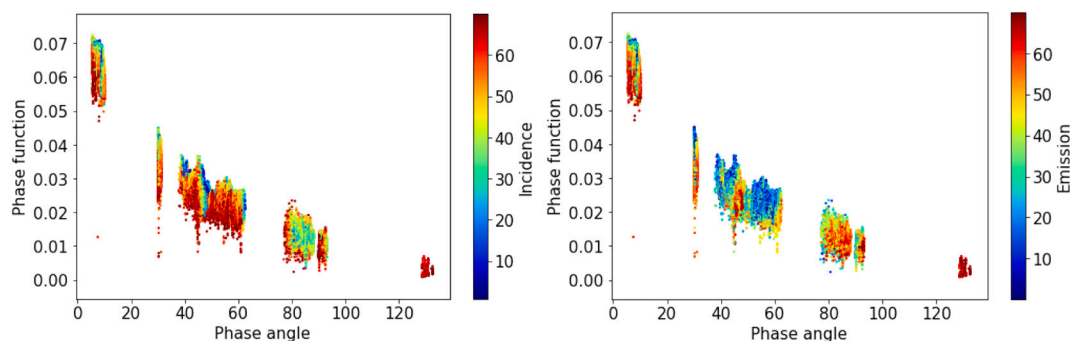


Fig. 6. The phase curve at $0.55 \mu\text{m}$, after application of a Lommel-Seeliger disk function correction, in which the phase function is RADF divided by that disk function. The spots are color-coded according to their incidence angle (left) and emission angle (right).

useful. These models have wide applications in photometry (e.g., Li et al. 2013, 2015; Takir et al. 2015; Schröder et al. 2017, 2013).

3.3. Modeling results

Our photometric modeling dataset (Sections 2.1 and 3.1) is the input for our model-fitting software. We employ a Levenberg–Marquardt least-squares minimization algorithm (Marquardt, 2009), and all OVIRS channels are fit independently. Fig. 7 shows the results for each model. The albedo parameter in each photometric model gradually decreases with wavelength, consistent with the “blue” color (spectral slope) of Bennu (Clark et al. 2011; Hamilton et al. 2019; Hergenrother et al. 2013). However, other model parameters show possible detector segment jumps at 0.6 , 1.1 , 1.7 , and $2.9 \mu\text{m}$ in the model parameter spectra, which are unphysical; the photometric parameters should be continuous across those wavelengths. Each filter segment shows a very slightly different trend in the spectra. For example, the segment from 1.7 to $2.7 \mu\text{m}$ shows a change in slope from positive to negative as compared with 2.7 to $3.7 \mu\text{m}$. The broad feature between 2.5 and $3.5 \mu\text{m}$ in the parameter spectra originates from the hydration band, remaining thermal tail and the behavior of the different filter segments. A few of the filter segment boundaries appear in the photometric models as very slight discontinuities. Some of the segment effects are due to how the detector is read during the spectrometer integration. The spacecraft scans the surface continuously as OVIRS acquires spectra. Even though the instrument is a point spectrometer, the detector reads out row by row, and each filter may integrate over slightly different areas on the surface. As a consequence, regions with shadows and/or regions close to the limb present some dark and some bright areas to the spectrometer, varying by filter segment as the integration proceeds in time.

When we model our observations, we implicitly assume that each OVIRS spectral channel is independent of its neighbors, and we fit each channel independently. This is not physically true, as explained in Reuter et al. (2018). As a result of our assumption, we find high-frequency “noise” in our best-fit model parameter spectra (blue lines in Fig. 7). We believe this is caused by the presence of several equally valid solutions to the fit, so the chi-square minimization oscillates between them. To remove this noise in the parameter spectra, we apply a smoothing procedure (Jones et al. 2001) to the model parameters that effectively results in averaging over the several valid solutions. We believe this to be the best way to account for the fact that each channel is not independent of its neighbors. We use a one-dimensional moving boxcar smoothing algorithm with box length 51, where we use the value of a best-fit third order polynomial within the box to replace the value at the center of the box. This smoothing procedure is applied to all parameters except for the albedo over the range from 0.4 to $3.7 \mu\text{m}$.

We calculated the RMS (root-mean-squared) values for each model (Fig. 8) against wavelength. All models have similar RMS trends, except for a difference in the overall level. Judging from the RMS plots, our McEwen and Minnaert models are similar and perform the best in terms

Table 2
Our suite of photometric models with their disk and phase functions in units of RADF.

Model*	Disk function	Phase function
Lommel-Seeliger (Hapke 2012)	$\pi A_{ls} \frac{\cos(i)}{\cos(i) + \cos(e)}$	$e^{\beta\alpha + \gamma\alpha^2 + \delta\alpha^3}$
Akimov (Shkuratov et al. 2011)	$\pi A_{ak} \cos\left(\frac{\alpha}{2}\right) \cos\left(\frac{\pi}{\pi - \alpha} \left(l - \frac{\alpha}{2}\right)\right) \left(\frac{\cos(b)\pi - \alpha}{\cos(l)}\right)$	$e^{\mu_1\alpha + \mu_2\alpha^2 + \mu_3\alpha^3}$
Linear-Akimov (Li et al. 2019)	$\pi A_{LiAk} \cos\left(\frac{\alpha}{2}\right) \cos\left(\frac{\pi}{\pi - \alpha} \left(l - \frac{\alpha}{2}\right)\right) \left(\frac{\cos(b)\pi - \alpha}{\cos(l)}\right)$	$10^{-0.4\beta\alpha}$
Minnaert (Minnaert 1941)	$\pi A_m \cos(i)^{k(\alpha)} \cos(e)^{k(\alpha)-1}$ $k(\alpha) = k_0 + b\alpha$	$10^{-0.4(\beta\alpha + \gamma\alpha^2 + \delta\alpha^3)}$
McEwen (McEwen 1986)	$\pi A_{mc} \left(2L(\alpha) \frac{\cos(i)}{\cos(i) + \cos(e)} + (1 - L(\alpha)) \cos(i) \right)$ $L(\alpha) = e^{\alpha + \zeta\alpha^2 + \eta\alpha^3}$	$e^{\beta\alpha + \gamma\alpha^2 + \delta\alpha^3}$

* note: Photometric model is the product of disk function and phase function.

Table 2
Comparison of albedo quantities for dark asteroids and comets.

	(1) Ceres Li et al. (2019)	(253) Mathilde Clark et al. (1999)	Phobos Simonelli et al. (1998)	Deimos Thomas et al. (1996)	9P/ Tempel 1 Li et al. (2013)	19P/ Borrelly Li et al. (2007)	81P/ Wild 2 Li et al. (2009)	28P/ Neujmin 1 Campins et al. (1987)	2P/ Encke Fernández et al. (2000)	(101955) Bennu
Geometric Albedo	0.096	0.047	0.071	0.068	0.059 ±	0.080 ±	0.059	0.026	0.05	0.049
Bolometric Bond Albedo	±0.006	±0.005	±0.012	±0.007	0.009	0.020	±0.004	±0.005	±0.02	±0.003
	0.037	–	0.021	0.027	0.014 ±	0.018	0.0093 and	–	–	0.025
	±0.002	–	±0.005	–	0.002	±0.001	0.012	–	–	±0.001

of describing the scattering properties of the Bennu surface. The Akimov model seems to show low RMS values, similar to the McEwen and Minnaert models, however according to goodness of fit criteria, McEwen is better than both Akimov and Minnaert. The Lommel-Seeliger model performs worse (about 20%). The Linear-Akimov model performs much worse (about 20% to 60%) than all the other models. The overall shapes of the RMS spectra are related to the signal-to-noise ratio of the input spectra, which depends on the original signal level on the detector. However, the segment boundary at 1.1 μm is visible in the parameter spectra for all models. This is an indication that part of the calibration process may not have fully accounted for all artifacts introduced during the observations: either out-of-band removal or changing scene during the spot integration (Simon et al. 2018).

We also evaluate the fit quality by comparing our modeled reflectance values with the measured values. Fig. 9 shows a typical goodness-of-fit plot for a single OVIRS channel using the McEwen model. We use these goodness-of-fit measurements to assess the fit quality by calculating the following proxies: (1) the correlation between the measured RADF and the modeled RADF, and the linear slope between them (Fig. 9, top left); and (2) the correlation and linear slope of the ratios between the measured and the modeled RADFs with respect to the three scattering angles (incidence, emission, phase; Fig. 9, top right, bottom right, and bottom left). A non-biased fit results in a correlation of 1 and a slope of 1 for the first proxy, and correlations of 0 and slopes of 0 for all the quantities in the second proxy. Any deviations from these values suggests a systematic error in the model. As such, for the fit to each spectral channel, eight proxies (four correlations and four slopes) are derived to quantify the quality of fit. We plot the eight quality proxies with respect to wavelength (Fig. 10) to help us assess which models perform the best in terms of capturing the scattering behavior of Bennu's surface. The Minnaert and McEwen models show overall better quality than the other models. The two Akimov models have a strong bias with respect to emission angle. The Lommel-Seeliger model has a strong bias against all three angles, indicating that this disk function is the worst at describing

the photometric behavior of Bennu's surface. The segment boundary at 1.1 μm is visible in the quality plot for all models.

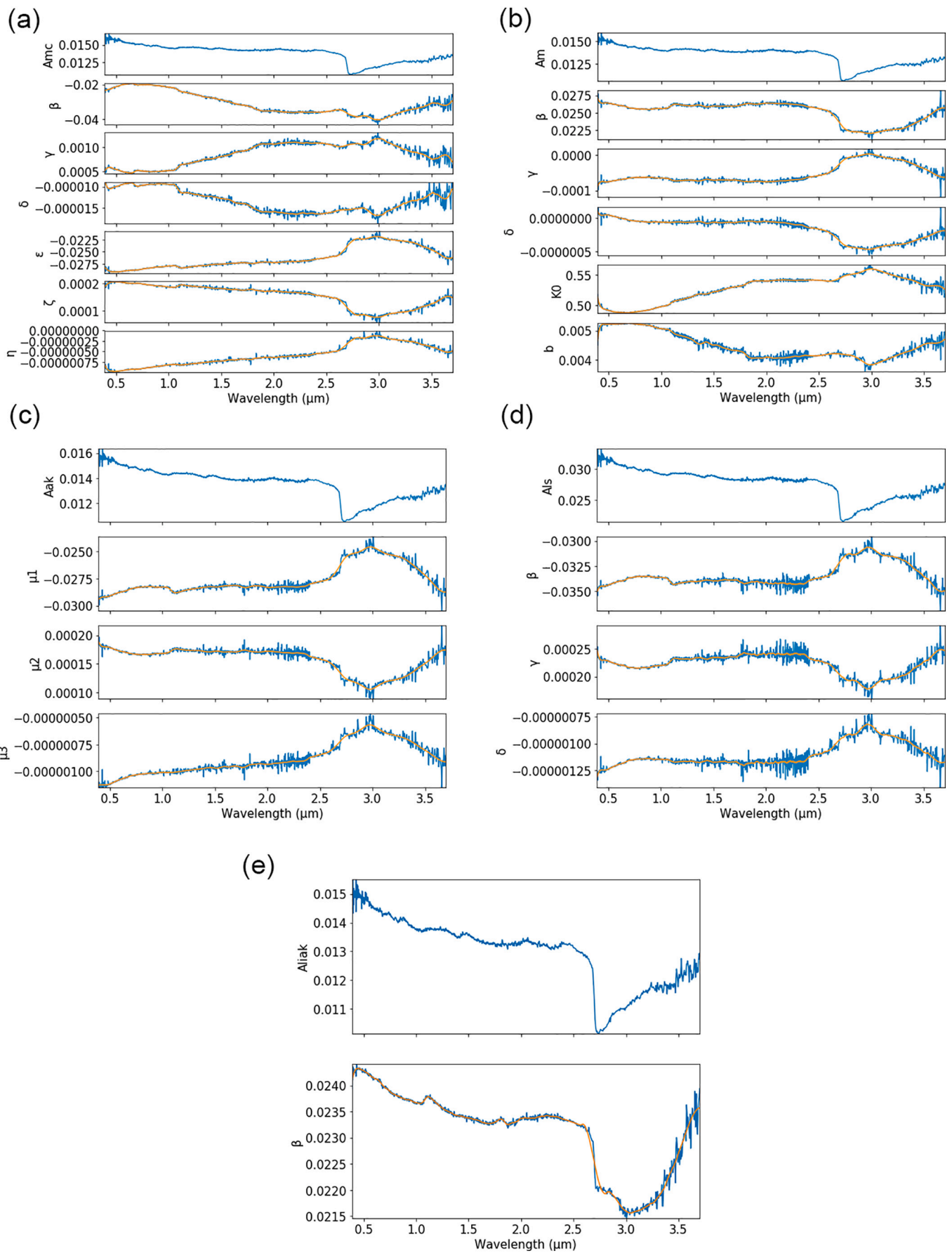
Once the RADF data from all spectral channels are fitted, we calculate the mean and standard deviation of the eight quality proxy spectra (Fig. 10) with respect to wavelength for all five photometric models (Lommel-Seeliger, McEwen, Minnaert, Akimov, and Linear-Akimov). Next we sum the larger of the absolute values of each pair of mean and standard deviation for each model. This sum for each model is used to evaluate the relative quality of the five models, and the model with the smallest quality value is designated the best model. The McEwen model (McEwen 1986) with an exponential phase function and an exponential polynomial partition function (a total of 7 free parameters) is the best fit for Bennu and we use this model in our assessments of the photometric properties of the surface.

3.4. Photometric correction

The spectral reflectance of Bennu's surface depends on the light-scattering geometry. To make comparisons between different areas and quantitatively interpret the spectra based on laboratory measurements, we must photometrically correct the observations to the same geometry. We choose a geometry commonly used in the laboratory setting, $(i_0, e_0, \alpha_0) = (30^\circ, 0^\circ, 30^\circ)$, for our default reference angles to facilitate direct comparisons with laboratory measurements of analog meteorites and mineral assemblages. Different researchers may use the photometric model equations in different ways. For example, correction to viewing geometry $(i_0, e_0, \alpha_0) = (0^\circ, 0^\circ, 0^\circ)$ is useful for subsequent calculation of the Bond albedo and for comparison with imaging data corrected to the same geometry (e.g. Golish et al. 2020).

The best-fit photometric model is used to correct all the RADF values of each spectral band to the reference angle:

$$r(i_0, e_0, \alpha_0) = \frac{r_{\text{model}}(i_0, e_0, \alpha_0)}{r_{\text{model}}(i, e, \alpha)} \times r(i, e, \alpha)$$



(caption on next page)

Fig. 7. Photometric model parameter spectra for each model. (a) McEwen model, (b) Minnaert model, (c) Akimov model, (d) Lommel-Seeliger model, (e) Linear-Akimov model. Each channel between 0.4 and 3.7 μm is independently fit, however parameter spectra (blue lines) are smoothed (yellow lines) with a one-dimensional boxcar algorithm with box length 51 and polynomial fit of order three before we use them for photometric corrections. These plots of our photometric models show the photometric parameter dependence on wavelength. They also show that model parameter spectra are very sensitive to absorption features, small jumps due to detector segment changes, and instrumental noise. It is interesting to note how model parameters trade off with one another across the wavelength range of the OVIRS data. We present all five of our models partly to facilitate comparisons other photometric studies of low-albedo asteroids. (For interpretation of the references to color in this figure legend, the reader is referred to the web version of this article.)

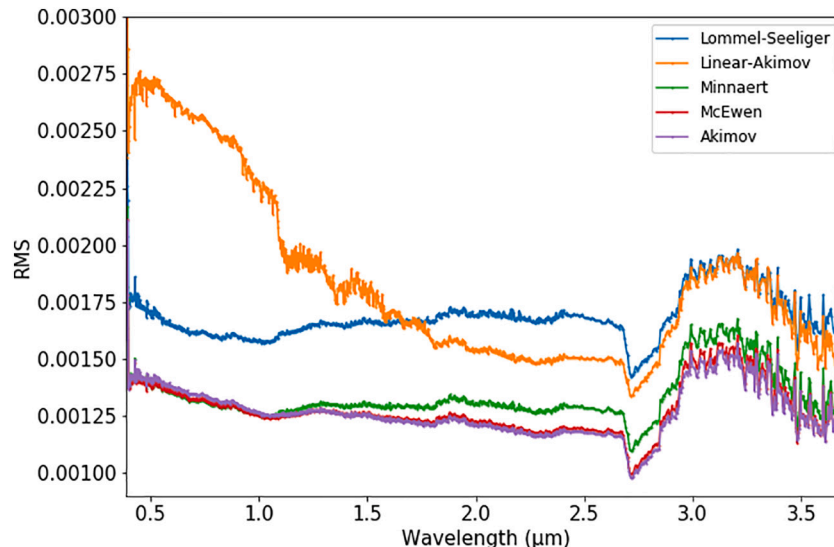


Fig. 8. RMS values capture the discrepancies between models and measurements as a function of wavelength for each model. The models with lowest RMS values are Akimov and McEwen, and this plot shows that they are slightly better than Minnaert, and much better than Lommel-Seeliger or Linear-Akimov.

where (i, e, α) is the scattering geometry of the measured reflectance. We demonstrated that our model is effective in correcting observations of the same spot viewed at different geometry to the same standard reference geometry. Fig. 11 shows a comparison of the spectra before and after photometric correction.

In order to visualize the spectral properties of Bennu, we mapped the photometrically corrected OVIRS data onto the three-dimensional Bennu shape model composed of triangular facets (Barnouin et al. 2019). The intersection of the OVIRS boresight with the shape model facets is calculated using the NAIF (Navigation and Ancillary Information Facility) SPICE toolkit (Acton 1996), such that the OVIRS spot data are mapped to the specific facets contained within the projected FOV of the spectrometer (Selznick 2017). The shape models used by the OSIRIS-REx mission have triangularly tessellated surfaces (Barnouin et al. 2020), where the ground sample distance represented by a facet decreases with improving knowledge of the shape of the asteroid. Because the shape model facets we use are small (80 cm in mean edge length), we sub-sample the OVIRS spots (there is an average of 113 facets per 20-m spot), the OVIRS data must be combined on a per-facet basis (Ferrone et al., 2019). We average together all OVIRS spots that cover a facet and assign the mean value to that facet. The resulting three-dimensional maps are shown in Fig. 12.

Variations in photometrically corrected albedo at 0.55 μm can be attributable to differences in both physical and compositional properties. For instance, the albedo at 0.55 μm of CI chondrites is generally lower than for CM chondrites (Cloutis et al. 2011a, 2011b), which differ in terms of their hydration state (CI's are more hydrated), particle size distribution (CI's have finer particles), and organic content (CM's have higher organic carbon abundance). Both of these meteorite types (Cloutis et al. 2012) have been suggested as possible analogs for Bennu (Hamilton et al. 2019). CI chondrites have reflectance values (in units of reflectance factor (REFF)) that range from 0.02 to 0.10 at the same viewing geometry ($30^\circ, 0^\circ, 30^\circ$) we use for photometric correction.

Converting RADF to REFF range equals 0.0238 to 0.0268. This range is slightly darker than the measured range of CM chondrite reflectances (0.03 to 0.11), albeit with substantial overlap (Clark et al. 2011). This may indicate that Bennu is more closely related to the CI chondrites than to the CMs, given that Bennu's reflectance (in units of REFF) ranges from 0.023 to 0.026 at 0.55 μm . However, because the two meteorite types, CI and CM, are so close to each other and overlap in observed reflectance ranges, this is not a decisive result (Clark et al. 2011). Albedo variations that occur across the surface of Bennu can be related to changes in physical properties, such as average particle size and the relative proportion of fines, (Cloutis et al. 2018; Kiddell et al. 2018); however, on Bennu there is a strong association between the darkest surface material and the presence of rough, hummocky (breccia-like) boulders, indicating that rock type seems to control albedo more strongly than particle size (DellaGiustina et al. 2020).

Fig. 13 shows the photometric model correction factor $\left(\frac{r_{\text{model}}(i_0, e_0, \alpha_0)}{r_{\text{model}}(i, e, \alpha)}\right)$ at the desired geometry) as a function of latitude. Although smooth variations are normal, we did not expect the strong wavelength dependence that we see in the correction factors calculated for higher latitudes. Bennu has a very rough and irregular surface, making the photometric correction factor uncertainties strongly latitude-dependent.

3.5. Bolometric Bond albedo map

With our photometric model, we can estimate the bolometric Bond albedo (A_{bolo}), an important value for understanding surface thermal properties. This albedo is the average spherical Bond albedo ($A_{\text{sph}}(\lambda)$) weighted by spectral irradiance of the Sun, $J_s(\lambda)$. This approach integrates spherical albedo over all relevant wavelengths, λ . Hence, we begin with a calculation of the spherical Bond albedo for each measured OVIRS spot:

The spherical bond albedo can be expressed as $q A_{\text{geo}}$, where q is phase integral, defined as:

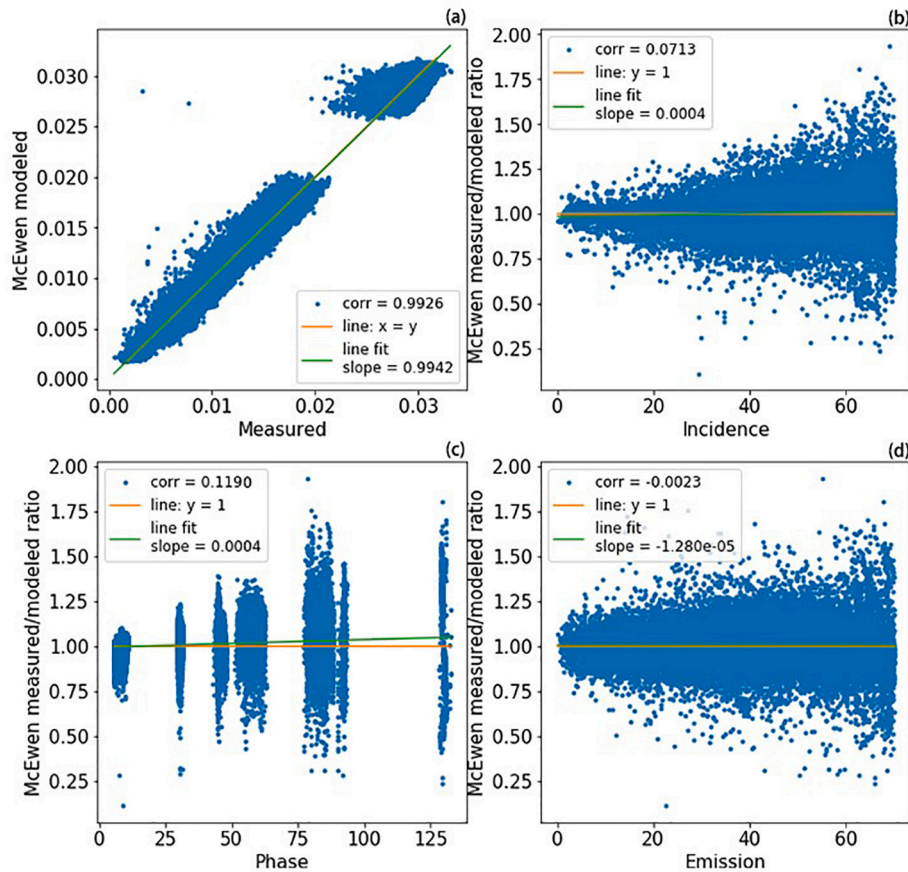


Fig. 9. Goodness of fit for the McEwen model. These are example goodness-of-fit plots to show how we calculate the quality values (correlation and slope) in the quality spectra shown in Fig. 10. (a) Modeled versus measured. (b) Ratio of measured/ modeled as a function of incidence angle. (c) Ratio of measured/ modeled as a function of phase angle. (d) Ratio of measured/ modeled as a function of emission angle.

$$q = 2 \int_0^\pi \Phi(\alpha) \sin(\alpha) d\alpha.$$

where $\Phi(\alpha) \equiv \frac{F(\alpha)}{F(0^\circ)}$ is the disk-integrated brightness at phase angle α , assuming a spherical body (Buratti and Veverka 1983), and normalized to unity at zero phase angle. $F(\alpha)$ is the phase dependence of the disk-integrated flux, defined as:

$$F(\alpha) = \frac{R^2}{r^2} \int_{\alpha-\frac{\pi}{2}}^{\frac{\pi}{2}} \int_{\alpha-\frac{\pi}{2}}^{\frac{\pi}{2}} \frac{I}{F} (i, e, \alpha) \cos(l) \cos^2(b) dl db,$$

where l is photometric longitude and b is photometric latitude.

Once we have the spherical bond albedo, we can calculate the bolometric Bond albedo. Strictly speaking, this quantity requires knowledge of the entire spectrum of the Sun and of Benu. However, because Benu’s spectrum is fairly neutral over most of the OVIRS wavelengths (except for near 2.74 μm , owing to the hydration band), and because solar spectral energy is mostly distributed in the visible to near-IR wavelengths, we can make a good approximation of the bolometric Bond albedo by integrating over the wavelengths of the OVIRS spectrometer, 0.4 to 3.7 μm .

$$A_{\text{bolo}} = \frac{\int_0^\infty A_{\text{sph}}(\lambda) J_S(\lambda) d\lambda}{\int_0^\infty J_S(\lambda) d\lambda}$$

Our bolometric Bond albedo map of Benu generated with the best-fit McEwen model is presented in Fig. 14. The global average bolometric Bond albedo of Benu is 0.025 ± 0.001 with a range of values from 0.021 to 0.027. The relative uncertainty in values that we calculate for bolometric Bond albedo ranges from 3.6% to 5.0% spatially, with an average of 3.7%. The bond albedo variations we observe across the surface are correlated with thermophysical properties of the boulders, as

described in Rozitis et al. (2020).

We compare our results for Benu with previously observed small dark bodies of the solar system in Table 2. Generally, Benu is darker than other asteroids, darker than the moons of Mars, and even darker than some comet nuclei. Presumably, this low albedo arises from Benu’s darker carbon-bearing organic species (Simon et al., 2020). In Section 4.3, we will discuss the special comparison between asteroids Ryugu and Benu.

3.6. Photometric uncertainty

In this section we discuss our estimate of the uncertainties of the photometric model. The OVIRS instrument systematic noise, the uncertainty of the thermal tail removal (TTR) process, and OVIRS detector segment boundaries all affect our model uncertainties.

The absolute radiometric calibration uncertainty is a systematic uncertainty affecting all the reflectance data by the same factor at each wavelength, and is independent of, and in addition to, the uncertainty analysis we present here (Reuter et al. 2018). However, the absolute radiometric uncertainty should only affect the various estimates of model albedo, but should not substantially affect the modeling of the disk and phase function–related parameters.

We believe that residuals from TTR may introduce uncertainties at wavelengths beyond 2.7 μm , as can be seen by the convex upward additional flux from 2.7 to 3.7 μm in the phase ratio in Fig. 1, and in the model fit RMS plot shown in Fig. 8. In addition, the latitude dependence shown in Fig. 1 is a clue that TTR assumptions may be affecting the spectra differentially. It is very difficult to quantitatively estimate the TTR-related uncertainty. But based on Fig. 8, the TTR uncertainties from

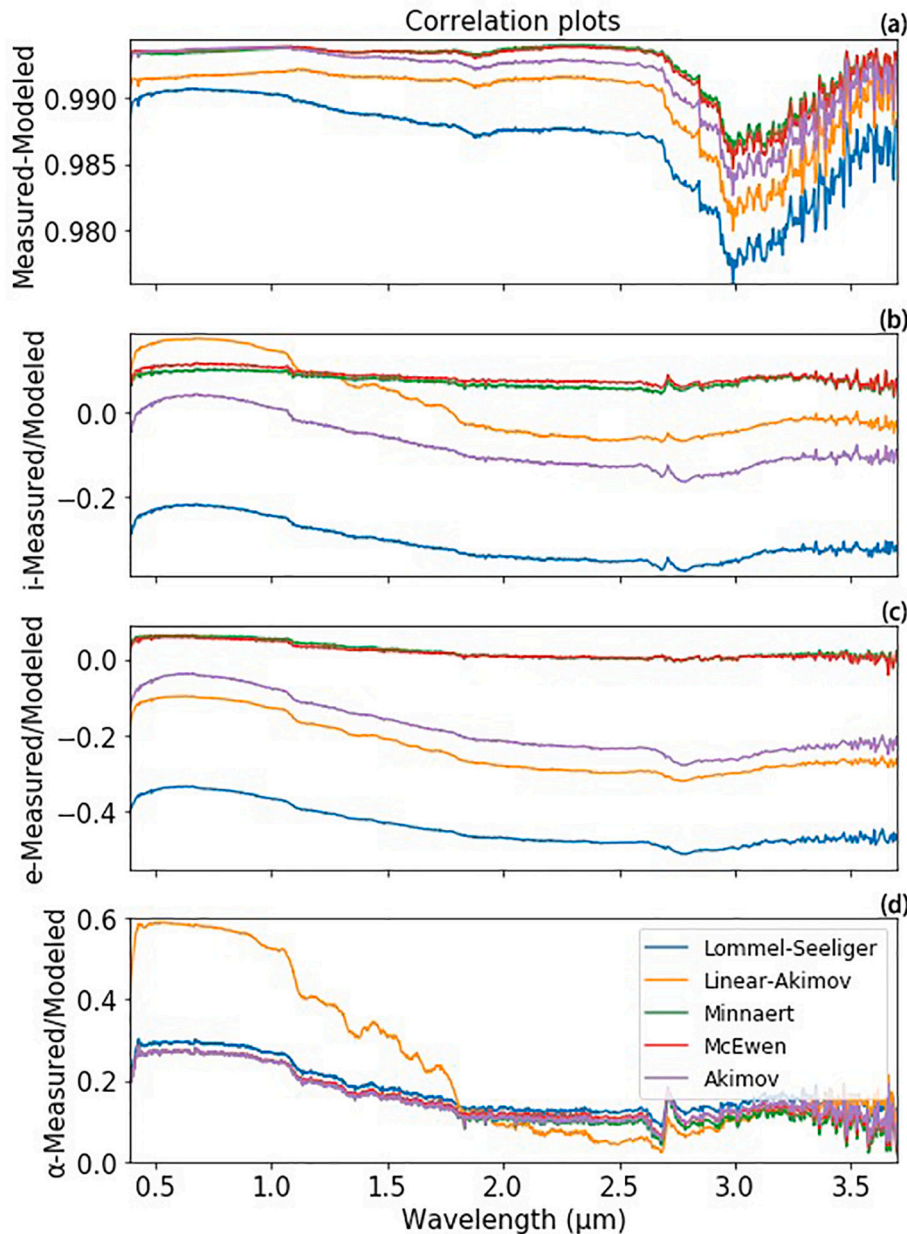


Fig. 10. Spectra of model quality proxies. Correlation plots: (a) A metric of the correlation between modeled and measured values (a correlation of 1.0 is best) and (b, c, d) measured/modeled ratio versus geometry (a value of 0.0 is best). Slope plots: (e) The slope of the line fit to modeled versus measured plots, and (f, g, h) the slope of the line fit to the measured/modeled ratio versus geometry (a value of 0.0 is best). These plots show that the McEwen and Minnaert models are closely similar in performance, and they are both higher in quality than the Akimov model in panels a, b, c, e, f, g. Considering this result together with the RMS comparisons in Fig. 8, we conclude that the McEwen model provides the best fit overall.

2.7 to 3.7 μm should be approximately of the same order as the radiometric noise uncertainties at shorter wavelengths. While we attempt to take these uncertainties into account when reporting our models and the uncertainty of the photometric correction, the strong latitude dependence and the strong wavelength dependence that we observe indicate that there are probably residual thermal effects in the input data, affecting the wavelengths from ~ 2.0 μm and above, and a full analysis of those higher-order uncertainties will require an extensive investigation of the geometric dependence of the thermal tail correction performed for OVIRS observations.

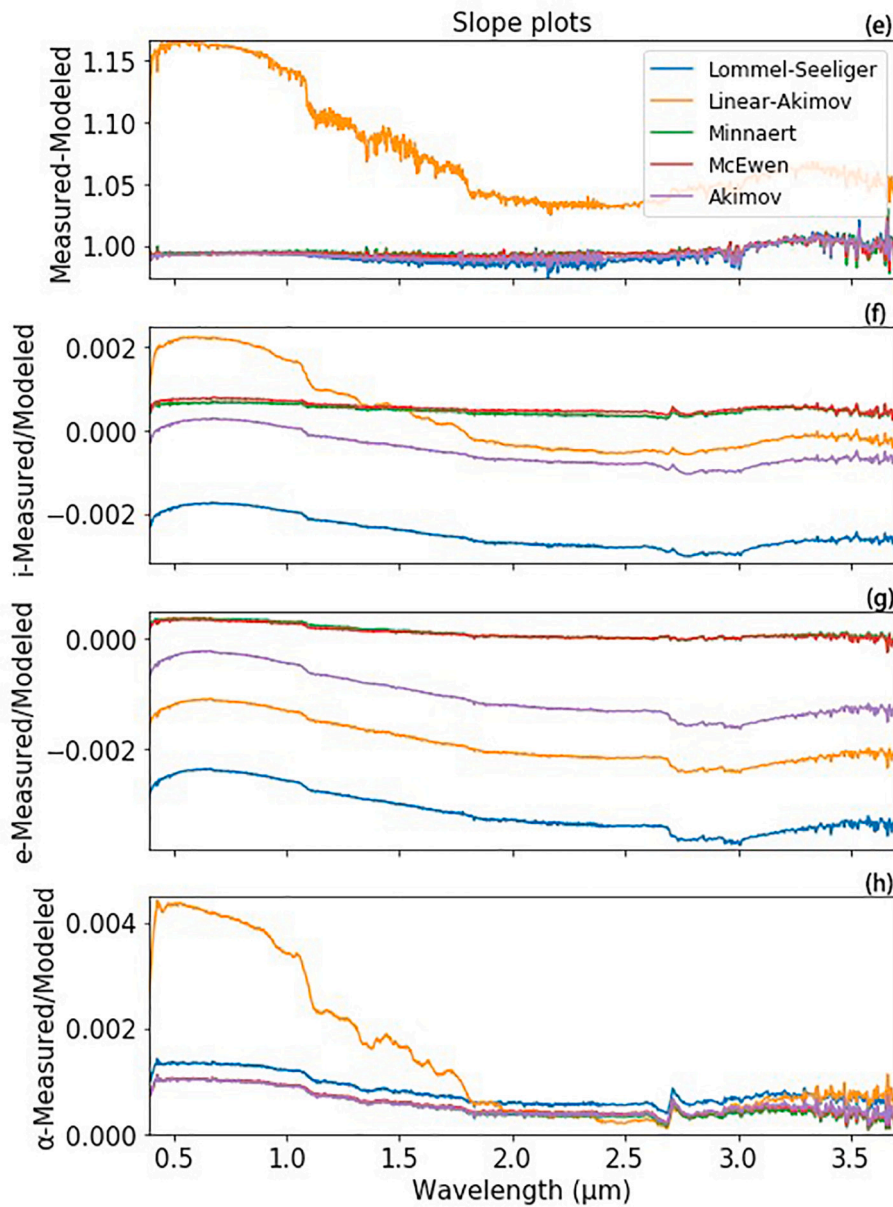
We paid close attention to the wavelength locations of detector segment boundaries, as these boundaries can impose artifacts on the OVIRS spectra because of the rolling nature of the shutter during an integration, especially at higher latitudes. When detector rows are read at slightly different times (a fraction of a second) during integrations across shadowed regions, different regions, and even Bennu's limb may be visible to different spectrometer segments as the spacecraft scans the surface at ~ 2 mrad/s. Photometric modeling is sensitive to the dependence on scattering geometry in the data and reflects segment

discontinuities (which are concentrated at higher latitudes) in the model quality and model parameters. While some segment boundaries remain detectable in our final photometric model parameter spectra, we have minimized their influence on our final product by rejecting those spots showing segment discontinuities of 10% or more. We cannot reject all spots showing the segment jump because they are from the higher latitudes, and these higher viewing and illumination geometries are important constraints on our model.

The uncertainty of the photometric model is propagated to the uncertainty of the photometric correction. There are three parts to photometric correction uncertainties: (1) noise in the measured signal, (2) model uncertainty in local geometry angles (i , e , α), as explained in section 3.4 regarding the strong latitude-dependence in our dataset and (3) model uncertainty at the reference geometry (i_0 , e_0 , α_0), (30° , 0° , 30°) in our case.

$$\sigma_{corr} = r_{corr} \sqrt{\left(\frac{[I/F]_{error}}{I/F}\right)^2 + \left(\frac{\sigma_{model}(30, 0, 30)}{\sigma_{model}(30, 0, 30)}\right)^2 + \left(\frac{\sigma_{model}}{\sigma_{model}(i, e, \alpha)}\right)^2}$$

Fig. 10. (continued).



where σ_{corr} is the photometric uncertainty in theory. I/F is the observation RADF, $[I/F]_{error}$ is the noise as describe above in (1), $\sigma_{model}(i, e, \alpha)$ is (2), $\sigma_{model}(30, 0, 30)$ is (3). Because the parameters of these photometric models are highly correlated, we need to use the covariance matrix derived for the parameters to calculate the partial derivatives array of the model parameters to estimate contributions from (2) and (3) above.

$$f(i, e, \alpha, a_1, a_2, \dots, a_n)$$

$$D = \begin{pmatrix} \frac{\partial f}{\partial a_1} \\ \frac{\partial f}{\partial a_2} \\ \vdots \\ \frac{\partial f}{\partial a_n} \end{pmatrix} \quad Cov = \begin{pmatrix} C_{11} & C_{12} & \dots & C_{1n} \\ C_{21} & C_{22} & \dots & C_{2n} \\ \vdots & \vdots & \ddots & \vdots \\ C_{n1} & C_{n2} & \dots & C_{nn} \end{pmatrix}$$

$$\sigma^2 = D^T Cov D$$

$$\sigma^2 = \begin{pmatrix} \frac{\partial f}{\partial a_1} & \frac{\partial f}{\partial a_2} & \dots & \frac{\partial f}{\partial a_n} \end{pmatrix} \begin{pmatrix} C_{11} & C_{12} & \dots & C_{1n} \\ C_{21} & C_{22} & \dots & C_{2n} \\ \vdots & \vdots & \ddots & \vdots \\ C_{n1} & C_{n2} & \dots & C_{nn} \end{pmatrix} \begin{pmatrix} \frac{\partial f}{\partial a_1} \\ \frac{\partial f}{\partial a_2} \\ \vdots \\ \frac{\partial f}{\partial a_n} \end{pmatrix}$$

where Cov is the covariance matrix from fitting result. Our analysis finds that both model error and noise in the measured signal are comparable contributions to the final correction error.

However, by smoothing the parameters according to wavelength (except for the albedo parameter) for each model, we reduce the model uncertainties by a factor equal to the square root of 51 (which is the window size of the smoothing, introduced in Section 3.3). This reduces model errors by one order of magnitude, to the point where they are negligible in terms of their contribution to the overall uncertainty. As a consequence, the uncertainties of the photometric correction depend

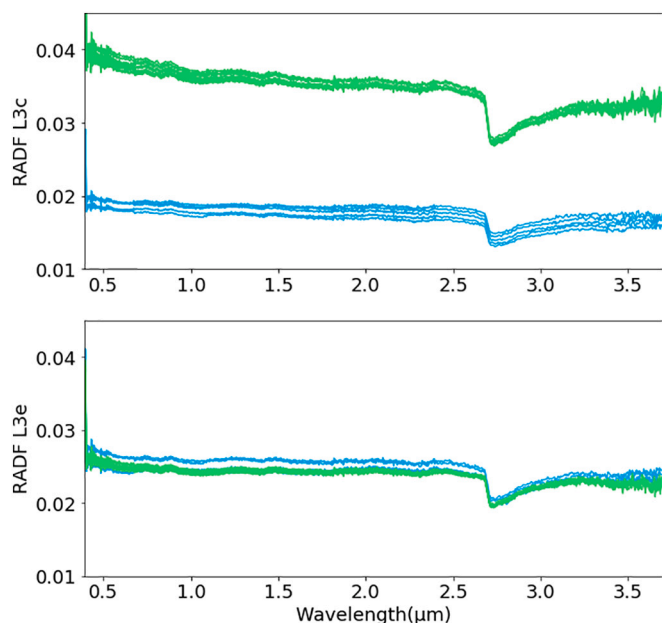


Fig. 11. Example of the comparison of spectra of Bennu obtained in a 10° by 10° area (center latitude, 60° ; longitude, 170°), before and after photometric correction (green is low phase angle and blue is high phase angle; both are observations of the same point on Bennu). Before photometric correction (top), spectra obtained at different viewing and illumination geometries of the same location differ strongly. After photometric correction (bottom), geometric effects have been removed, and the spectra are consistent. (For interpretation of the references to color in this figure legend, the reader is referred to the web version of this article.)

only on propagated noise in the measured signal.

$$error = \sigma \frac{r_{model}(i_0, e_0, \alpha_0)}{r_{model}(i, e, \alpha)}$$

where σ is the noise in the measured signal directly from the calibrated level 3 RADF results. And $error$ is the value we propagate to the 2-D array of uncertainties in the photometric correction results.

This uncertainty includes absolute radiometric uncertainty and calibration error (Simon et al. 2018). In sum, we estimate the relative error in our photometric correction to be $\pm 5.6\%$ at $0.55 \mu\text{m}$. Uncertainties at other wavelengths are comparable. The relative 1-sigma error in the global bolometric Bond albedo is $\pm 3.7\%$.

4. Phase reddening and comparison with other minor bodies

In this section, we analyze the phase reddening effects we observe in the spectral observations of Bennu, and we compare our photometric modeling results with those from other asteroids and comets.

4.1. Phase reddening

We analyzed the dependence of our derived phase functions with respect to wavelength (Fig. 7e shows the most direct measure of this dependence). The slope of the phase function with respect to phase angle, or phase slope (Fig. 15), is shallower at longer wavelengths, indicative of phase reddening. The results show phase reddening of 17% from 0.4 to $2.7 \mu\text{m}$, but no reddening longward of that. One possible cause of the cessation of phase reddening at around $2.7 \mu\text{m}$ is that between 2.0 and $3.7 \mu\text{m}$, the thermal component of the measurement of Bennu's radiance starts to dominate. It is estimated that at $3.4 \mu\text{m}$ at EQ2 and EQ6 on Bennu, almost 85% of the measured radiance is due to thermal emission, not reflected radiance (Simon et al., 2020).

The magnitude of the phase slope on Bennu is slightly lower than for

typical comets and dark asteroids, which have slopes of 0.04 mag/deg. (Hergenrother et al. 2013). Previously published results (Golish et al. 2020; DellaGiustina and Emery et al., 2019) have shown Bennu's phase reddening from multicolor images ranging in wavelength from 0.47 to $0.85 \mu\text{m}$, consistent with our result. Phase reddening could be evidence for multiple scattering, roughness, or the characteristics of single-particle scattering (Li et al. 2019).

4.2. Comparison with OCAMS and ground-based observations

Golish et al. (2020) draw no conclusions with regard to Bennu's photometric disk function, as they find that all model results are very close together, within the noise. Golish et al. find that their model phase functions agree (roughly) with the ground-based predictions, but not exactly; they find more phase reddening and a slightly stronger opposition surge in the Bennu imaging data. To compare the photometric properties from OVIRS with results from OCAMS (Golish et al. 2020), we averaged OVIRS channels to match the equivalent OCAMS bandwidth (Table 3) to simulate OCAMS low-spectral-resolution data. To match the range of phase angles of the OCAMS observations, we discarded all data collected at 3 am local solar time (EQ2 and EQ6; phase angle $\sim 130^\circ$) and re-ran the photometric modeling routine. Table 3 lists the wavelength sampling that we performed to select the OVIRS channels most comparable with OCAMS bandpasses. In Fig. 16 we compare the phase function of model results from both the OCAMS and OVIRS datasets. We note that Golish et al. 2020 averaged each whole image into one measurement in their photometric analysis, so what we are comparing here differs in spatial sampling (OCAMS at ~ 400 m/data point, OVIRS at ~ 20 m/data point). Compared in this manner, the models show no large differences, indicating that these two instruments generally agree with each other in the way that they capture Bennu's relative photometric behavior, except that the OVIRS flux models generally predict a higher value (by $\sim 9\%$) than the OCAMS models.

As an example, we compare the OVIRS and OCAMS flux models for Bennu at $0.55 \mu\text{m}$. First, we assume that the difference between geometric albedo and normal radiance factor at $(0^\circ, 0^\circ, 0^\circ)$ is negligible. Then, according to OVIRS, Bennu's average geometric albedo = 0.048 with a standard deviation = 0.003, so to within one sigma, 68% of Bennu's surface falls in the range 0.045 to 0.051. By comparison, according to OCAMS (DellaGiustina et al., 2020), Bennu's average geometric albedo = 0.044 with a standard deviation = 0.005, so to within one sigma, 68% of Bennu's surface falls in the range 0.039 to 0.049. At this wavelength, the OVIRS model predicts that Bennu is 8.7% brighter than the OCAMS model predicts. We note that this is consistent in sense and order of magnitude with an offset between OVIRS and the OSIRIS-REx Thermal Emission Spectrometer (OTES), reported by Rozitis et al. (2020), where again, OVIRS predicts a slightly higher thermal flux by about 7%. The discrepancies between instruments are thus about 8% on average, possibly reflecting the difficulty in measuring these quantities accurately, or possibly reflecting the effects of differences in spatial resolution.

In Fig. 16 we also compare the OVIRS photometry results with the ground-based predictions from Takir et al. 2015 for Bennu's phase function in terms of the Lommel-Seeliger model. The OVIRS results are in generally good agreement with the ground-based observations within the uncertainties in the ground-based models. The slightly steeper slope in the ground-based phase function over OVIRS's phase function is also noticed by Golish et al. (2020).

4.3. Comparison with (162173) Ryugu

The Hayabusa2 mission performed close-up observations of (162173) Ryugu, an asteroid with many similarities to Bennu (Sugita et al. 2019). Examination of the visible wavelength properties, based on data obtained with the Telescopic Optical Navigation Camera (ONC-T) system, show that Ryugu, like Bennu, is a very dark object; it has a

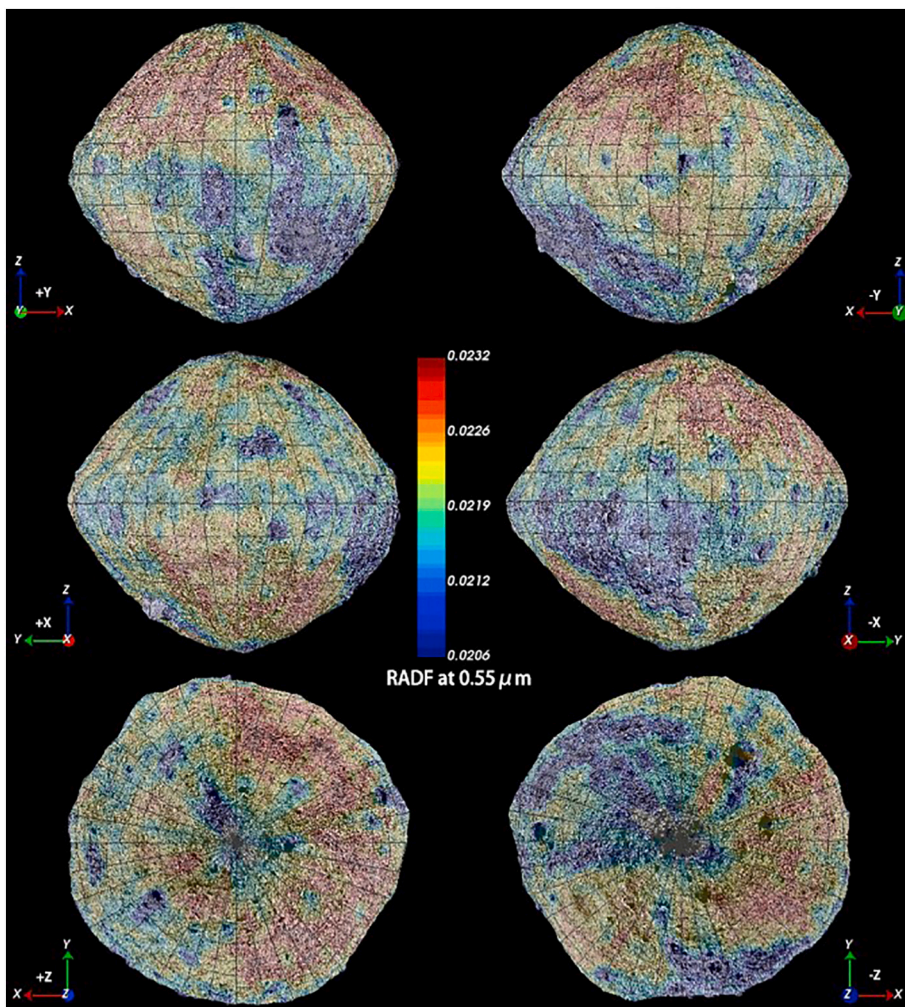


Fig. 12. A global 3D facet-based map of the photometrically corrected (to 30°, 0°, 30°) OVIRS spots at a wavelength of 0.55 μm. The data are overlain on the OCAMS imaging basemap (Bennett et al. 2020), as viewed in the Small Body Mapping Tool (Ernst et al. 2018). Input spectra were obtained during Detailed Survey EQ3.

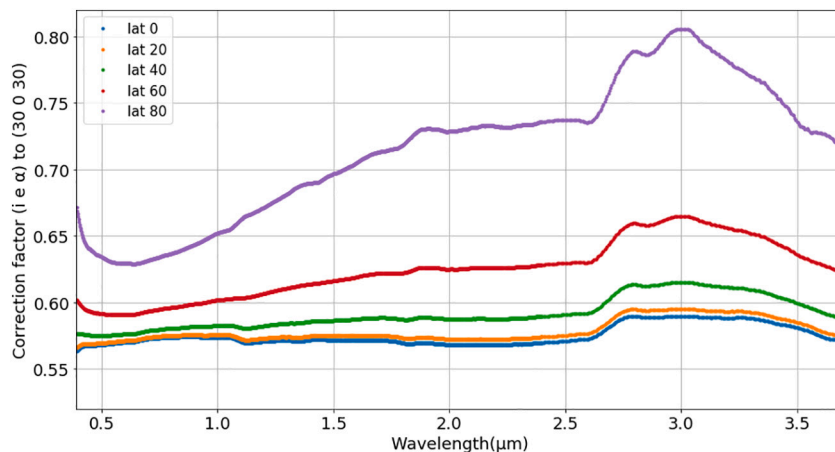


Fig. 13. Photometric correction factor. The correction factor is applied from phase angle 8° to phase angle 30° for spectra obtained at various latitudes from 0° (equatorial) to 80° (close to the poles).

geometric albedo of 0.040 ± 0.005 at $0.55 \mu\text{m}$ (Tatsumi et al. 2020) compared to a geometric albedo of 0.049 ± 0.003 at $0.55 \mu\text{m}$ for Bennu (calculated using our OVIRS McEwen model equations). The disk-integrated Bond albedo calculated from the ONC observations is constant from $0.48 \mu\text{m}$ to $0.95 \mu\text{m}$ at 0.014 ± 0.01 (Tatsumi et al. 2020),

compared to the spatial range of bolometric Bond albedo values from 0.021 to 0.027 for Bennu. Notice that the bolometric Bond albedo of Bennu is an integrated quantity, calculated assuming the OVIRS wavelength range from 0.4 to 3.7 captures most of the reflected light from Bennu. The shape of Ryugu’s reflectance spectrum is flat, whereas the

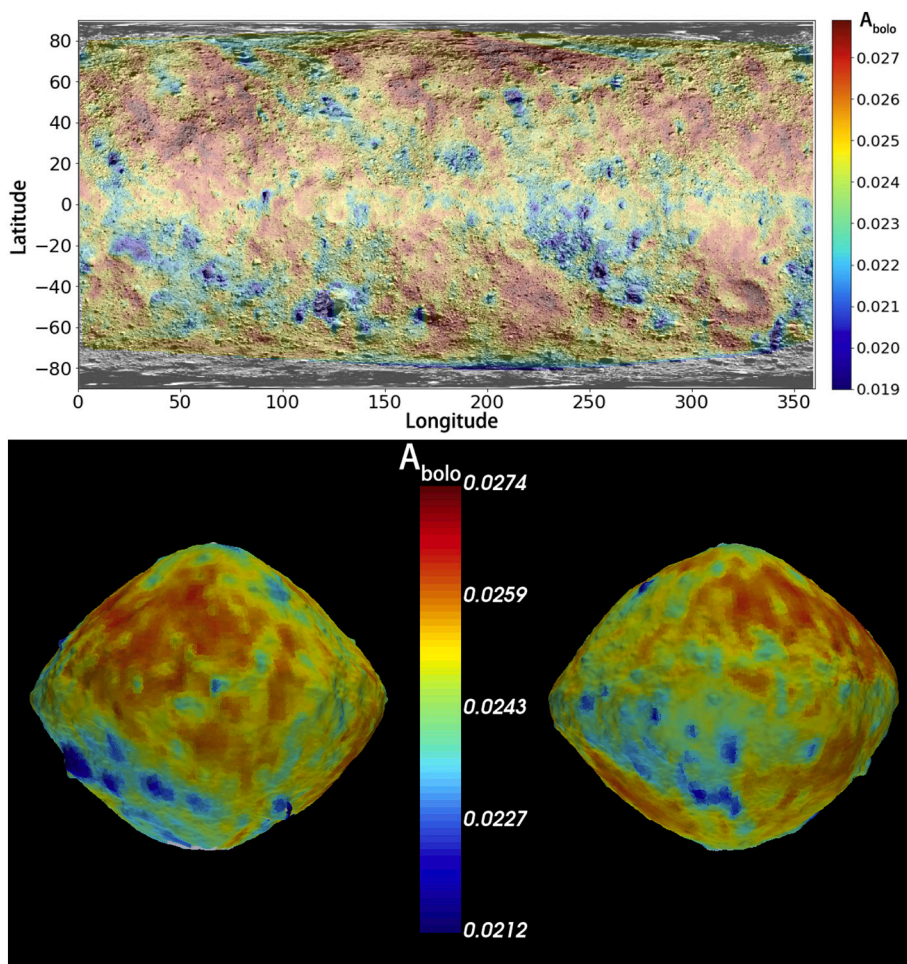


Fig. 14. Bolometric Bond albedo using the best-fit McEwen model. (Top) A global linear-interpolated latitude-longitude map of bolometric Bond albedo, overlain on the global OCAMS basemap (Bennett et al. 2020). (Bottom) A global three-dimensional map of bolometric Bond albedo, as viewed in the Small Body Mapping Tool (Ernst et al. 2018).

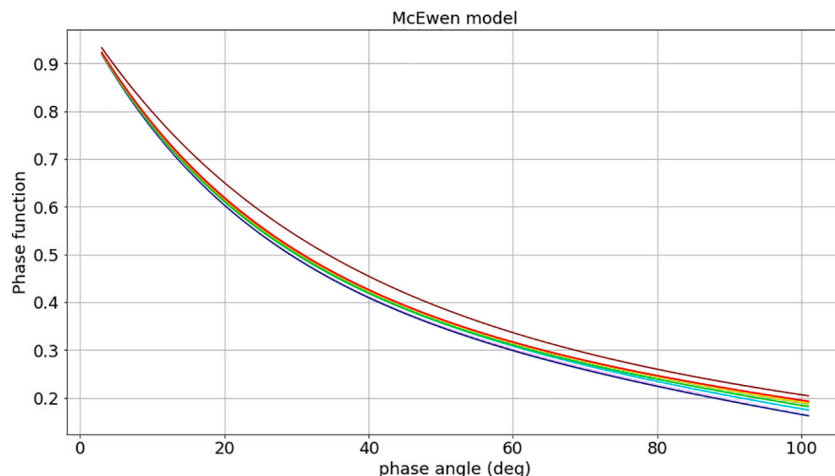


Fig. 15. Comparison of McEwen model phase functions of 11 OVIRS channels. Rainbow-colored: violet to maroon corresponding to short wavelength (0.4 μm) to long wavelength (3.7 μm). (For interpretation of the references to color in this figure legend, the reader is referred to the web version of this article.)

shape of Bennu’s reflectance spectrum is sloping down towards longer wavelengths (blue). For Ryugu, Tatsumi et al. (submitted) report an average reflectance factor at 0.55 μm of 0.0187 ± 0.0014 , after standardization to (30°, 0°, 30), with all reflectance factor variations occurring to within $\pm 10\%$, over the whole surface (Tatsumi et al.

submitted).

In the visible and near-infrared wavelengths, Ryugu’s spectra are slightly red (Sugita et al. 2019, Kitazato et al. 2019, Tatsumi et al. submitted, Domingue et al. in prep, meaning that reflectance increases as wavelength increases. Examination of Bennu’s global spectrum

Table 3
OVIRS channel averages comparable with OCAMS bandpasses at similar wavelength ranges.

OCAMS broad band filter*	Effective wavelength (μm)	Number of OVIRS channels equivalent to OCAMS band	Start equivalent wavelength (μm)	Starting OVIRS channel	End equivalent wavelength (μm)	Ending OVIRS channel
pan	0.646	128	0.519	65	0.773	191
b'	0.473	41	0.445	28	0.501	55
v	0.550	80	0.521	66	0.579	94
w	0.698	154	0.667	138	0.729	170
x	0.847	228	0.808	209	0.885	248

* pan stands for panchromatic, and the other filter names come from ECAS Eight Color Asteroid Survey filters (Rizk et al. 2018).

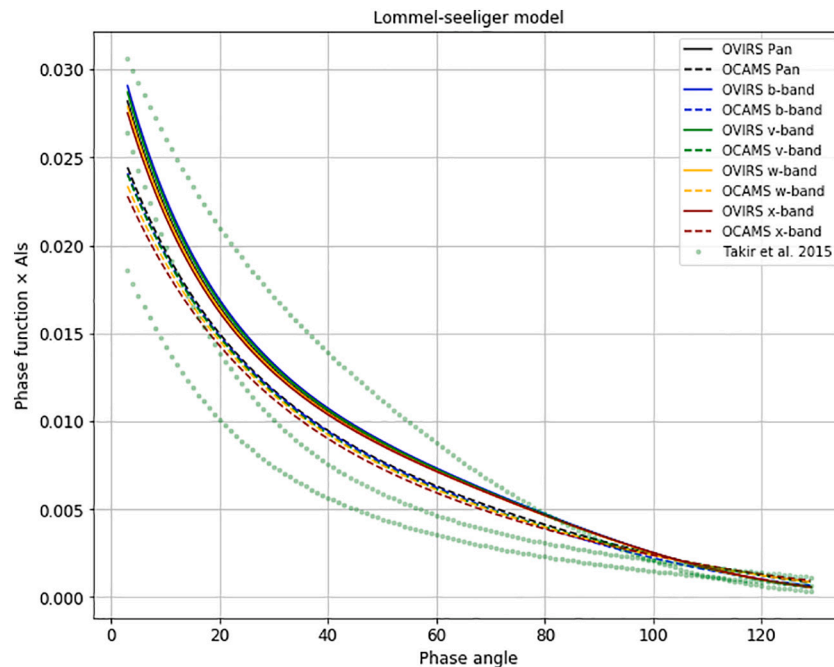


Fig. 16. Comparison of Lommel-Seeliger model results, in terms of phase function, for the OCAMS and OVIRS datasets and the ground-based predictions (nominal, maximum, and minimum) of Takir et al. (2015).

reveals that, in contrast, Bennu's surface is mostly spectrally blue (reflectance decreases with increasing wavelength) (Hamilton et al. 2019). In a study of various particle sizes of the Murchison meteorite, Binzel et al. (2015) showed that coarse-grained samples (500 to 1000 μm) are spectrally blue, but the addition of 5% of fine-grained sample ($<45 \mu\text{m}$) shifts the spectral slope from blue to red. In other words, the inclusion of a fine-grained fraction introduces spectral reddening (Schröder et al. 2014; Binzel et al. 2015). Studies of carbonaceous chondrites show that increasing the average grain size shifts spectra to being darker and more blue-sloped (Johnson and Fanale 1973; Cloutis et al. 2011b, 2013; Gillis-Davis et al. 2013; Binzel et al. 2015). Therefore, the spectral slope differences between Bennu and Ryugu could be interpreted to suggest that the regolith on Bennu is possibly coarser, lacking a finer-particulate component that seems to be present on Ryugu.

According to our photometric models, Bennu has a phase reddening of about $(4.16 \pm 0.08) \times 10^{-4} \mu\text{m}^{-1} \text{deg.}^{-1}$ from 0.48 μm to 2.5 μm , compared to the stronger phase reddening seen on Ryugu of $(2.0 \pm 0.7) \times 10^{-3} \mu\text{m}^{-1} \text{deg.}^{-1}$ from 0.48 μm to 0.86 μm (Tatsumi et al. submitted). When we measure the visible range for phase reddening, from 0.48 to 0.86 μm , we find phase reddening about $(1.525 \pm 0.002) \times 10^{-3} \mu\text{m}^{-1} \text{deg.}^{-1}$ in the results for Bennu. But this measurement may include an error introduced by the segment jump at 0.66 μm . Because the phase reddening of Bennu is weak, it could be very sensitive to uncertainties in the model. Thus, we can only conclude here that both Bennu and Ryugu

show weak phase reddening.

When we examine the model spectral slope as a function of incidence angle at a common phase angle, we find no clear segregation of slope with incidence angle. This is interesting because the laboratory work by Potin et al. (2019) demonstrated such a correlation in spectral slope with incidence for slab or rock samples of the CM2 meteorite Mukundpura, but no correlation for powdered samples of the same meteorite. The lack of correlation of model spectral slope with incidence angles may indicate that Bennu has a granular component at the surface. The spectrometer footprint size in this OVIRS study ranges from 40 to 15 m. This implies that down to 15-m resolutions, there may be a granular regolith component (microns to 100 μm in size) present at some portion of this footprint resolution. Particles covering part (not all) of the surface could be sufficient to affect the photometric properties. However, the composition of these two asteroids is different (Hamilton et al. 2019; Kitazato et al. 2019), which could also cause different spectrophotometric behavior.

5. Summary and conclusions

We have presented the global average photometric modeling results of asteroid Bennu with data acquired by the OVIRS spectrometer onboard the OSIRIS-REX spacecraft. We constrained our models with data from flybys and equatorial station observations performed during the Preliminary Survey and Detailed Survey mission phases. We retrieved

the radiance factor of all selected spots; paired them with their respective geometry, time, and spot quality information; and fit the data with our suite of photometric models. We found that a McEwen model (McEwen 1986) with an exponential phase function and an exponential polynomial partition function (a total of 7 free parameters) is the best fit for Bennu. We used this model to correct the OVIRS spectra of Bennu to a standard reference viewing and illumination geometry of $(i, e, \alpha) = (30^\circ, 0^\circ, 30^\circ)$ at visible to infrared wavelengths. From our best-fit model, we produced a bolometric Bond albedo map; values for Bennu's surface range from 0.021 to 0.027. A measure of the global bolometric Bond albedo is useful for inferring the distribution of thermal energy across the surface, which affects dehydration, thermal fatigue, and other thermal processes in the regolith. A phase reddening effect of about $(4.16 \pm 0.08) \times 10^{-4} \mu\text{m}^{-1} \text{deg.}^{-1}$ is evident between 0.48 and 2.5 μm , with no reddening beyond those wavelengths, and our model is effective at removing it. We found that Bennu has a blueish spectrum, consistent with telescope-based observations. A $> 10\%$ absorption feature is centered at 2.74 μm .

By comparing our results with the OCAMS results reported by Golish et al. (2020), we found that the OVIRS phase function is approximately 9% brighter than the OCAMS Bennu phase function, due probably to the different absolute radiometric calibrations between the two instruments. We also found general agreement between OVIRS results and the ground-based predictions reported by Takir et al. (2015). By comparison with carbonaceous meteorites and other low-albedo solar system bodies, we find that Bennu's albedo range is similar to that of CI chondrites and is darker than most asteroids, both moons of Mars, and some comet nuclei, potentially due to the presence of carbon. Finally, we compare the surface properties of Bennu with those of asteroid (162173) Ryugu observed by the Hayabusa2 spacecraft. We find that Bennu is a few percent brighter than Ryugu in the visible wavelengths, and both Ryugu and Bennu have very weak phase reddening (Tatsumi et al. 2020). More detailed comparisons with Ryugu should be possible in the future, when the NIRS3 (Near-InfraRed Spectrometer 3) photometric modeling results are available.

Declaration of Competing Interest

None.

Acknowledgements

This material is based upon work supported by NASA under Contract NNM10AA11C issued through the New Frontiers Program. We are grateful to the entire OSIRIS-REx Team for making the encounter with Bennu possible and the exploration highly successful. X.-D. Zou and J.-Y. Li also acknowledge partial support from the Solar System Exploration Research Virtual Institute 2016 (SSERVI16) Cooperative Agreement (Grant NNH16ZDA001N), SSERVI-TREX to the Planetary Science Institute. M. A. Barucci acknowledges funding support from CNES. We also thank Heather Roper for providing the mission phase observational strategy figure.

Data Availability

OVIRS [Level 3c] data (inputs to our modeling) are available in the Planetary Data System at <https://sbn.psi.edu/pds/resource/orex/ovirs.html> (Reuter et al. 2019). Data are delivered to the PDS according to the schedule in the OSIRIS-Rex Data Management Plan (<https://sbnarchive.psi.edu/pds4/orex/orex.mission.document/>) (Crombie and Selznick, 2019).

Appendix A. Supplementary data

Supplementary data to this article can be found online at <https://doi.org/10.1016/j.icarus.2020.114183>.

References

- Selznick, S.H., 2017. An Architecture for Real-Time Processing of OSIRIS-REx Engineering and Science Data, from Raw Telemetry to PDS. Third Planetary Data Workshop and The Planetary Geologic Mappers Annual Meeting, 2017, 1986.
- Simon, et al., 2020. Widespread carbon-bearing materials on near-earth asteroid (101955) Bennu. Science. <https://doi.org/10.1126/science.abc3522>.
- DellaGiustina, et al., 2020. Variations in Color and Reflectance on the surface of Asteroid (101955) Bennu. Science. <https://doi.org/10.1126/science.abc3660>.
- Ernst, et al., 2018. The Small Body Mapping Tool (SBMT) for Accessing, Visualizing, and Analyzing Spacecraft Data in Three Dimensions, LPSC 49, abstract no. 1043.
- Tatsumi, et al., 2020. Global photometric properties of (162173) Ryugu. <https://doi.org/10.1051/0004-6361/201937096>.
- Acton, C.H., 1996. Ancillary Data Services of NASA's Navigation and Ancillary Information Facility. Planetary and Space Science 44 (1), 65–70. [https://doi.org/10.1016/0032-0633\(95\)00107-7](https://doi.org/10.1016/0032-0633(95)00107-7).
- Barnouin, O.S., Daly, M.G., Palmer, E.E., Gaskell, R.W., Weirich, J.R., Johnson, C.L., Al Asad, M.M., Roberts, J.H., Perry, M.E., Susorney, H.C.M., Daly, R.T., Bierhaus, E.B., Seabrook, J., Espiritu, R.M., Nair, A.H., Nguyen, L., Neumann, G.A., Ernst, C.M., Boynton, W.V., Nolan, M.C., Adam, C., Moreau, M.C., Risk, B., D'Aubigny, C., Javin, E.R., Walsh, K.J., Michel, P., Schwartz, S.R., Ballouz, R.L., DellaGiustina, D.N., Mazarico, E.M., Scheeres, D.J., McMahon, J., Bottke, W., Sugita, S., Hirata, N., Watanabe, S., Lauretta, D.S., 2019. Shape of (101955) Bennu indicative of a rubble pile with internal stiffness. Nature Geoscience 12 (4), 247–252. <https://doi.org/10.1038/s41561-019-0330-x>.
- Barnouin, O.S., Daly, M.G., Palmer, E.E., Johnson, C.L., Gaskell, R.W., Al Asad, M., Bierhaus, E.B., Craft, K.L., Ernst, C.M., Espiritu, R.C., Nair, H., Neumann, G.A., Nguyen, L., Nolan, M.C., Mazarico, E., Perry, M.E., Philpott, L.C., Roberts, J.H., Steele, R.J., Lauretta, D.S., 2020. Digital terrain mapping by the OSIRIS-REx mission. Planetary and Space Science 180. <https://doi.org/10.1016/j.pss.2019.104764> [104764].
- Bennett, C.A., et al., 2020. A high-resolution global basemap of (101955) Bennu. Icarus. <https://doi.org/10.1016/j.icarus.2020.113690>.
- Binzel, Richard P., DeMeo, Francesca E., Burt, Brian J., Cloutis, Edward A., Rozitis, Ben, Burbine, Thomas H., Campins, Humberto, Clark, Beth Ellen, Emery, Joshua P., Hergenrother, Carl W., Howell, Ellen S., Lauretta, Dante S., Nolan, Michael C., Mansfield, Megan, Pietrasz, Valerie, Polishook, David, Scheeres, Daniel J., 2015. Spectral slope variations for OSIRIS-REx target Asteroid (101955) Bennu: Possible evidence for a fine-grained regolith equatorial ridge. Icarus 256, 22–29. <https://doi.org/10.1016/j.icarus.2015.04.011>. ISSN 0019-1035.
- Buratti, B., Veverka, J., 1983. Voyager photometry of Europa. Icarus 53, 93–110. [https://doi.org/10.1016/0019-1035\(83\)90053-2](https://doi.org/10.1016/0019-1035(83)90053-2).
- Campins, H., A'Hearn, M.F., McFadden, L.A., 1987. The bare nucleus of comet Neujmin 1. Astrophys. J. 316, 847–857. <https://doi.org/10.1086/165249>.
- Clark, B.E., Veverka, J., Helfenstein, P., Thomas, P.C., Bell III, J.F., Harch, A., Robinson, M.S., Murchie, S.L., McFadden, L.A., Chapman, C.R., 1999. NEAR photometry of asteroid 253 Mathilde. Icarus 140, 53–65. <https://doi.org/10.1006/icar.1999.6124>.
- Clark, B.E., Binzel, R.P., Howell, E., Cloutis, E.A., Ockert-Bell, M.E., Christensen, P., Barucci, M.A., DeMeo, F., Lauretta, D., Connolly Jr., H., Soderberg, A., Hergenrother, C., Lim, L., 2011. Asteroid (101955) 1999 RQ36: spectroscopy from 0.4 to 2.4 μm and meteorite analogs. Icarus 216 (2), 462–475. <https://doi.org/10.1016/j.icarus.2011.08.021>.
- Cloutis, E.A., Hudon, P., Hiroi, T., Gaffey, M.J., Mann, P., 2011a. Spectral reflectance properties of carbonaceous chondrites: 1. CI chondrites. Icarus 212 (1), 180–209. <https://doi.org/10.1016/j.icarus.2010.12.009>.
- Cloutis, E.A., Hudon, P., Hiroi, T., Gaffey, M.J., Mann, P., 2011b. Spectral reflectance properties of carbonaceous chondrites: 2. CM chondrites. Icarus 216 (1), 309–346. <https://doi.org/10.1016/j.icarus.2011.09.009>.
- Cloutis, E.A., et al., 2012. Spectral reflectance properties of carbonaceous chondrites 4: Aqueously altered and thermally metamorphosed meteorites. Icarus 220 (2), 586–617. <https://doi.org/10.1016/j.icarus.2012.05.018>.
- Cloutis, E.A., et al., 2018. Spectral reflectance “deconstruction” of the Murchison CM2 carbonaceous chondrite and implications for spectroscopic investigations of dark asteroids. Icarus 305, 203–224. <https://doi.org/10.1016/j.icarus.2018.01.015>.
- Crombie, M.K., Selznick, S., 2019. Origins, spectral interpretation, resource identification, security, regolith explorer (OSIRIS-REx): Mission bundle, urn:nasa:pds:orex.Mission. NASA Planetary Data System.
- DellaGiustina, D.N., Emery, J.P., Golish, D.R., Rozitis, B., Bennett, C.A., Burke, K.N., Ballouz, R.-L., Becker, K.J., Christensen, P.R., Drouot d'Aubigny, C.Y., Hamilton, V. E., Reuter, D.C., Rizk, B., Simon, A.A., Asphaug, E., Bandfield, J.L., Barnouin, O.S., Barucci, M.A., Bierhaus, E.B., Binzel, R.P., Bottke, W.F., Bowles, N.E., Campins, H., Clark, B.C., Clark, B.E., Connolly, H.C., Daly, M.G., de Leon, J., Delbo, M., Deshpriya, J.D.P., Elder, C.M., Fornasier, S., Hergenrother, C.W., Howell, E.S., Javin, E.R., Kaplan, H.H., Kareta, T.R., Le Corre, L., Li, J.-Y., Licandro, J., Lim, L.F., Michel, P., Molero, J., Nolan, M.C., Pajola, M., Popescu, M., Garcia, J.L.R., Ryan, A., Schwartz, S.R., Shultz, N., Siegler, M.A., Smith, P.H., Tatsumi, E., Thomas, C.A., Walsh, K.J., Wolner, C.W.V., Zou, X.-D., Lauretta, D.S., 2019. Properties of rubble-pile asteroid (101955) Bennu from OSIRIS-REx imaging and thermal analysis. Nature Astronomy 3 (4), 341–351. <https://doi.org/10.1038/s41550-019-0731-1>.
- Fernández, Y.R., Lisse, C.M., Käufel, H.U., Peschke, Sibylle B., Weaver, H.A., A'Hearn, M. F., Lamy, P.L., Livengood, T.A., Kostiuik, T., 2000. Physical properties of the nucleus of comet 2P/Encke. Icarus 147, 145–160. <https://doi.org/10.1006/icar.2000.6431>.
- Ferrone, S., et al., December 2019. Analysis of Projection Effects in OSIRIS-REx Spectral Mapping Methods: Recommended Protocols and Spectral Super-Resolution. Submitted spring 2019 to Earth and Space Science, Revision Submitted.

- Gillis-Davis, Jeffrey J., et al., 2013. Laser space weathering of Allende meteorite. LPI 1719 2494. <https://www.lpi.usra.edu/meetings/lpsc2013/pdf/2494.pdf>.
- Golish, D.R., et al., 2020. Disk-resolved photometric modeling and properties of asteroid (101955) Benu. *Icarus*. <https://doi.org/10.1016/j.icarus.2020.113724>.
- Hamilton, V.E., et al., 2019. Evidence for widespread hydrated minerals on asteroid (101955) Benu. *Nature Astronomy* 3 (4), 332–340. <https://doi.org/10.1038/s41550-019-0722-2>.
- Hapke, B., 2012. *Theory of Reflectance and Emittance Spectroscopy* (Cambridge University Press).
- Hasselmann, P.H., Fornasier, S., Barucci, M.A., Praet, A., Clark, B.E., Li, J.-Y., Golish, D. R., DellaGiustina, D.N., Deshapriya, J.D.P., Zou, X.-D., Daly, M.G., Barnouin, O.S., Lauretta, D.S., 2020. Modeling optical roughness and first-order scattering processes from OSIRIS-REx color images of the rough surface of asteroid (101955) Benu. *Icarus*, 114106. <https://doi.org/10.1016/j.icarus.2020.114106>. ISSN 0019-1035.
- Hergenrother, C.W., et al., 2013. Lightcurve, color and phase function photometry of the OSIRIS-REx target asteroid (101955) Benu. *Icarus* 226 (1), 663–670. <https://doi.org/10.1016/j.icarus.2013.05.044>.
- Johnson, Torrence V., Fanale, Fraser P., 1973. Optical properties of carbonaceous chondrites and their relationship to asteroids. *J. Geophys. Res.* 78 (35), 8507–8518. <https://doi.org/10.1029/JB078i035p08507>.
- Jones, E., Oliphant, T., Peterson, P., 2001. *SciPy: Open Source Scientific Tools for Python*.
- Kiddell, C.B., et al., 2018. Spectral reflectance of powder coatings on carbonaceous chondrite slabs: implications for asteroid regolith observations. *Journal of Geophysical Research: Planets* 123 (10), 2803–2840. <https://doi.org/10.1029/2018JE005600>.
- Kitazato, K., et al., 2019. The surface composition of asteroid 162173 Ryugu from Hayabusa2 near-infrared spectroscopy. *Science* 364 (6437), 272–275. <https://doi.org/10.1126/science.aav7432>.
- Kreslavsky, M.A., Head III, J.W., 2000. Kilometer scale roughness of Mars: results from MOLA data analysis. *Journal of Geophysical Research: Planets* 105 (E11), 26695–26711. <https://doi.org/10.1029/2000JE001259>.
- Lauretta, D.S., et al., 2017. OSIRIS-REx: sample return from asteroid (101955) Benu. *Space Sci. Rev.* 212 (1–2), 925–984. <https://doi.org/10.1007/s11214-017-0405-1>.
- Li, J.-Y., A'Hearn, M.F., McFadden, L.A., Belton, M.J.S., 2007. Photometric analysis and disk-resolved thermal modeling of comet 19P/Borely from deep space 1. *Icarus* 188, 195–211. <https://doi.org/10.1016/j.icarus.2006.11.015>.
- Li, J.-Y., A'Hearn, M.F., Farnham, T.L., McFadden, L.A., 2009. Photometric analysis of the nucleus of comet 81P/wild 2 from stardust images. *Icarus* 204, 209–226. <https://doi.org/10.1016/j.icarus.2009.06.002>.
- Li, J.-Y., A'Hearn, M.F., Belton, M.J.S., Farnham, T., Klaasen, K.P., Sunshine, J.M., Thomas, P.C., Veverka, J., 2013. Photometry of the nucleus of comet 9P/Tempel 1 from stardust-NExT flyby and the implications. *Icarus* 222, 467–476. <https://doi.org/10.1016/j.icarus.2012.02.011>.
- Li, J.-Y., et al., 2019. Spectrophotometric modeling and mapping of Ceres. *Icarus* 322, 144–167. <https://doi.org/10.1016/j.icarus.2018.12.038>.
- Li, J.-Y., et al., 2020. Corrigendum to “asteroid photometry” [asteroids IV (2015)(P. Michel et al., eds.), pp. 129–150]. *Icarus* 337. <https://doi.org/10.1016/j.icarus.2019.06.015>, 113354.
- Markwardt, C.B., 2009 Feb 17. Non-linear least squares fitting in IDL with MPFIT. *arXiv preprint arXiv:0902.2850*.
- McEwen, A.S., 1986. Exogenic and endogenic albedo and color patterns on Europa. *Journal of Geophysical Research: Solid Earth* 91 (B8), 8077–8097. <https://doi.org/10.1029/JB091iB08p08077>.
- Minnaert, M., 1941. The reciprocity principle in lunar photometry. *Astrophys. J.* 93, 403–410.
- Potin, S., Beck, P., Schmitt, B., Moynier, F., 2019. Some things special about NEAs: Geometric and environmental effects on the optical signatures of hydration. *Icarus* 333, 415–428. <https://doi.org/10.1016/j.icarus.2019.06.026>. ISSN 0019-1035.
- Reuter, D.C., et al., 2018. The OSIRIS-REx visible and InfraRed spectrometer (OVIRS): spectral maps of the asteroid Benu. *Space Sci. Rev.* 214 (2), 54. <https://doi.org/10.1007/s11214-018-0482-9>.
- Reuter, D.C., et al., 2019. Origins, spectral interpretation, resource identification, security, regolith explorer (OSIRIS-REx): visible and InfraRed spectrometer (OVIRS) bundle, urn:NASA:pds:orex.Ovirs, NASA planetary data system.
- Rizk, B., et al., 2018. OCAMS: the OSIRIS-REx camera suite. *Space Sci. Rev.* 214 (1), 26. <https://doi.org/10.1007/s11214-017-0460-7>.
- Rozitis, B., et al., 2020. Asteroid (101955) Benu's weak boulders and thermally anomalous equator. *Sci. Adv.* <https://doi.org/10.1126/sciadv.abc3699>.
- Schröder, S.E., et al., 2013. Resolved photometry of Vesta reveals physical properties of crater regolith. *Planet. Space Sci.* 85, 198–213. <https://doi.org/10.1016/j.pss.2013.06.009>.
- Schröder, S.E., Mottola, S., Keller, H.U., Raymond, C.A., Russell, C.T., 2014. Reprint of: Resolved photometry of Vesta reveals physical properties of crater regolith. *Planet. Space Sci.* 103, 66–81. <https://doi.org/10.1016/j.pss.2014.08.001>. ISSN 0032-0633.
- Schröder, S.E., et al., 2017. Resolved spectrophotometric properties of the Ceres surface from Dawn framing camera images. *Icarus* 288, 201–225. <https://doi.org/10.1016/j.icarus.2017.01.026>.
- Shkuratov, Y., et al., 2011. Optical measurements of the moon as a tool to study its surface. *Planetary and Space Science* 59 (13), 1326–1371. <https://doi.org/10.1016/j.pss.2011.06.011>.
- Simon, A.A., et al., 2018. In-flight calibration and performance of the OSIRIS-REx visible and IR spectrometer (OVIRS). *Remote Sens.* 10 (9), 1486. <https://doi.org/10.3390/rs10091486>.
- Simonelli, D., et al., 1998. Photometric properties of Phobos surface materials from Viking images. *Icarus* 131, 52–77. <https://doi.org/10.1006/icar.1997.5800>.
- Sugita, Satoshi, et al., 2019. The geomorphology, color, and thermal properties of Ryugu: Implications for parent-body processes. *Science* 364, 6437. <https://doi.org/10.1126/science.aaw0422>.
- Takir, D., et al., 2015. Photometric models of disk-integrated observations of the OSIRIS-REx target asteroid (101955) Benu. *Icarus* 252, 393–399. <https://doi.org/10.1016/j.icarus.2015.02.006>.
- Thomas, P.C., Adinolfi, D., Helfenstein, P., Simonelli, D., Veverka, J., 1996. The surface of Deimos: contribution of materials and processes to its unique appearance. *Icarus* 123, 536–556. <https://doi.org/10.1006/icar.1996.0177>.